

1 **Perineuronal Net Formation and the Critical Period for Neuronal Maturation in the**
2 **Hypothalamic Arcuate Nucleus**

3

4 Zaman Mirzadeh¹, Kimberly M. Alonge², Elaine Cabrales¹, Vicente Herranz-Pérez^{4,5},
5 Jarrad M. Scarlett^{2,3}, Jenny M. Brown², Rim Hassouna⁶, Miles E. Matsen², Hong T.
6 Nguyen², Jose Manuel Garcia-Verdugo⁴, Lori M. Zeltser^{6,7}, and Michael W. Schwartz²

7

8 ¹Department of Neurosurgery, Barrow Neurological Institute, Phoenix, AZ, USA.

9 ²Diabetes Institute, School of Medicine, University of Washington, Seattle, WA, USA.

10 ³Department of Pediatric Gastroenterology and Hepatology, Seattle Children's Hospital,
11 Seattle, WA, USA.

12 ⁴Laboratory of Comparative Neurobiology, Instituto Cavanilles, CIBERNED, Universidad
13 de Valencia, 46980 Valencia, Spain.

14 ⁵Predepartmental Unit of Medicine, Faculty of Health Sciences, Universitat Jaume I,
15 12071 Castelló de la Plana, Spain.

16 ⁶Naomi Berrie Diabetes Center, ⁷Department of Pathology and Cell Biology, Columbia
17 University, New York, NY, USA.

18

19 *Corresponding Authors:

20 Michael W. Schwartz, MD

21 Professor and RH Williams Endowed Chair in Medicine

22 Co-Director, Diabetes Institute, University of Washington School of Medicine

23 850 Republican Street, Box 358055, Seattle, WA 98109

24 mschwart@uw.edu

25

26 Zaman Mirzadeh, MD PhD

27 Assistant Professor, Department of Neurosurgery

28 Barrow Neurological Institute, St. Joseph's Hospital and Medical Center

29 350 W. Thomas Rd., Phoenix, AZ 85013

30 zaman.mirzadeh@barrowneuro.org

31

32 **Keywords:** neural plasticity, critical period, perineuronal net, arcuate nucleus, energy
33 balance, glucose homeostasis

34 **Acknowledgements:**

35 The authors are grateful to the original providers of the transgenic mouse lines used in
36 this work: Nobuaki Tamamaki (GAD67-GFP)¹, Martin Myers (LepRb-Cre)², Hongkui
37 Zeng (Ai14)³, Bradford Lowell (Npy-GFP)⁴, and Malcolm Low (POMC-GFP)⁵. This work
38 was supported by the US NIH National Institute of Diabetes and Digestive and Kidney
39 Diseases (grant nos. DK108596 (Z.M.), DK114474 (J.M.S.), DK083042 (M.W.S.),
40 DK090320 (M.W.S.), and DK101997 (M.W.S.)), National Institute of Neurological
41 Disorders and Stroke Neurosurgeon Research Career Development Program K Award
42 (Z.M.), the American Diabetes Association (grant no. 7-11-BS-179 (L.Z.)), the Russell
43 Berrie Foundation (R.H.), and the Barrow Neurological Foundation (Z.M.).

44

45

46

47 **Summary**

48 In leptin-deficient *ob/ob* mice, obesity and diabetes are associated with abnormal
49 development of neurocircuits in the hypothalamic arcuate nucleus (ARC), a critical brain
50 area for energy and glucose homeostasis. As this developmental defect can be
51 remedied by systemic leptin administration, but only if given before postnatal day 28, a
52 critical period (CP) for leptin-dependent development of ARC neurocircuits has been
53 proposed. In other brain areas, CP closure coincides with the appearance of
54 perineuronal nets (PNNs), extracellular matrix specializations that restrict the plasticity
55 of neurons that they enmesh. We report that in humans as well as rodents, key subsets
56 of ARC neurons are enmeshed by PNNs. In mice, most of these neurons are both
57 GABAergic and leptin receptor-positive, including a large subset of *Agrp* neurons, and
58 the postnatal appearance of these PNNs coincides precisely with both closure of the CP
59 for ARC neuron development and maturation of *Agrp* neuron projections. Moreover,
60 postnatal PNN formation is impaired in the ARC of leptin-deficient *ob/ob* mice, and this
61 defect is rescued by leptin administration during the CP. In contrast, PNN density is
62 increased in the ARC of adult *ob/ob* mice, potentially owing to the increased activity of
63 *Agrp* neurons in the absence of leptin. Collectively, these findings implicate PNN
64 formation in the control of ARC neuron development and show that PNN formation in
65 this brain area is dependent on input from circulating leptin. Aberrant PNN formation in
66 the ARC of animals predisposed to obesity and diabetes offers a plausible link between
67 ARC neurocircuit dysfunction and the pathogenesis of common metabolic disorders.

68

69

70 During critical periods (CPs) of early postnatal life, developing neurocircuits are
71 exquisitely sensitive to and shaped by external cues from the environment⁶. The CP for
72 ocular dominance plasticity in primary visual cortex (V1) is a well-studied example:
73 during the CP, but not before or after, visual deprivation of one eye induces a strong
74 shift of neuronal responses to the non-deprived eye⁷. The associated loss of acuity in
75 the deprived eye, clinically referred to as amblyopia, is difficult to remedy after CP
76 closure.

77 In diverse neurocircuits ranging from the mammalian visual, barrel
78 (somatosensory) and entorhinal cortices to the hippocampus and amygdala, and in
79 song nuclei in the songbird brain as well, CP closure is dependent on the formation of
80 perineuronal nets (PNNs)⁸⁻¹⁵. PNNs are extracellular matrix specializations composed
81 largely of hyaluronan and chondroitin sulfate proteoglycans that enmesh primarily
82 inhibitory interneurons^{10,16}. Remarkably, experimentally disrupting PNNs in adult
83 animals is capable of reactivating CP plasticity in these diverse brain areas. In V1, for
84 example, PNN digestion enables restoration of vision to a previously deprived eye⁸.
85 Comparable restorative effects of PNN disruption are reported across neurological and
86 psychiatric disorders as diverse as PTSD, depression, drug addiction and spinal cord
87 injury^{10,16,17}.

88 Recently, compelling evidence was provided in support of the existence of a CP
89 for the maturation of Agouti-related peptide (Agrp) neurons in the hypothalamic arcuate
90 nucleus (ARC)¹⁸. As key regulators of feeding behavior, Agrp neurons are among the
91 best-studied of all hypothalamic neurons. These GABAergic neurons co-express the
92 potent orexigen neuropeptide Y (NPY), and they project to downstream targets in

93 homeostatic circuits governing energy balance and glucose homeostasis. Maturation of
94 these projections occurs during the lactation period, concomitant with a naturally-
95 occurring leptin surge (P4-P14)^{19,20}, and this maturation process appears to be
96 dependent on leptin since these projections fail to develop properly in leptin-deficient
97 *ob/ob* mice (a genetic model of obesity and type 2 diabetes (T2D)). Moreover, this
98 defect in *Agrp* neuron development can be rescued by treatment with exogenous leptin,
99 but only if administered before P28^{18,19,21}. A CP for the trophic action of leptin on *Agrp*
100 neuron maturation therefore exists, and its closure coincides with both the transition to
101 independent feeding and maturation of the cellular response of *Agrp* neurons to input
102 from leptin²². This CP is also a uniquely sensitive time when both over- and
103 undernutrition predispose to obesity and glucose intolerance in adulthood²³⁻²⁷.

104 Here we show that PNNs enmesh key subpopulations of ARC neurons in
105 humans as well as rodents. These neurons are predominantly GABAergic and many are
106 leptin-receptor positive, including a majority of *Agrp* neurons. In mice, PNN formation in
107 this region coincides with both maturation of *Agrp* neuron projections and closure of the
108 CP for *Agrp* neuron development. Our finding of altered ARC PNNs in developing and
109 adult mouse models of obesity and type 2 diabetes points to a potential role for PNNs in
110 aberrant development and/or altered plasticity of ARC neurocircuits in common
111 metabolic diseases.

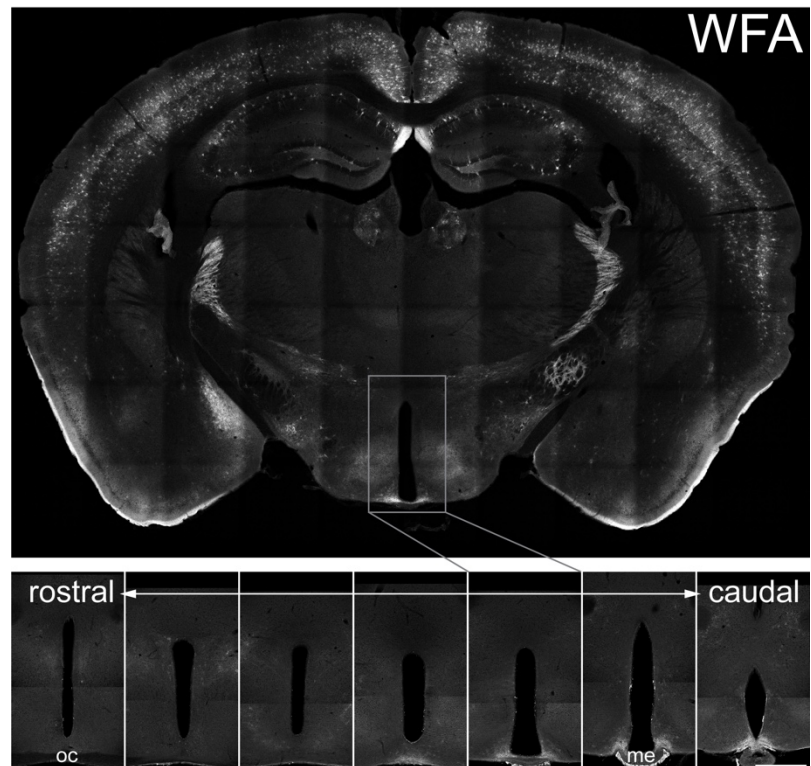
112

113 **Results**

114 We performed immunohistochemistry (IHC) on serial coronal sections of mouse
115 hypothalamus using *Wisteria floribunda* agglutinin, a lectin that selectively labels the *N-*

116 acetylgalactosamine residue on chondroitin sulfate (CS) chains in PNNs. Our initial
117 survey (**Supplementary Fig 1**) revealed numerous PNN-enmeshed cells localized to
118 the junction of the ARC and median eminence (ME) (**Fig 1a-d**). Compared to the rather
119 sparse distribution of PNN-enmeshed neurons in most brain areas (e.g., V1), enmeshed
120 cells in the ARC-ME area are densely packed (**Fig 1e, g**). To better characterize the
121 structural features of these cells, we used high-resolution confocal microscopy
122 combined with Imaris image analysis of individually-labelled, PNN-enmeshed neurons
123 located at the periphery of the dense cluster at the ARC-ME junction. Analysis of these
124 cells (**arrow f in Fig 1c**) allowed us to better define the anatomical relationship between
125 PNNs and the neurons they enmesh without the confounding influence of labeling on an
126 adjacent, closely apposed cell. As expected, PNNs enwrap both cell soma and
127 proximal processes (**Fig 1f**), reminiscent of PNN structures described in the visual
128 cortex (**Fig 1g,h**).

129 Wholemount preparations of
130 the mediobasal hypothalamus,
131 stained with WFA and imaged
132 from either the ventricular
133 surface (**Fig 1i**) or the ventral
134 pial brain surface (**Fig 1j**),
135 revealed the presence of a
136 continuous “collar” of PNN-
137 enmeshed cells at the junction
138 of the ARC and ME.



Supplementary Figure 1. Tiled panoramic confocal image of a coronal section at the level of the ARC stained with WFA (top), and corresponding serial coronal sections through the hypothalamus from the optic chiasm (oc) to the infundibular recess (bottom row), reveal a specific concentration of PNN enmeshed cells in the ventromedial ARC at its junction with the ME. Scale bar: 500 μ m. Images are representative of data from at least 5 animals.

139
140
141
142

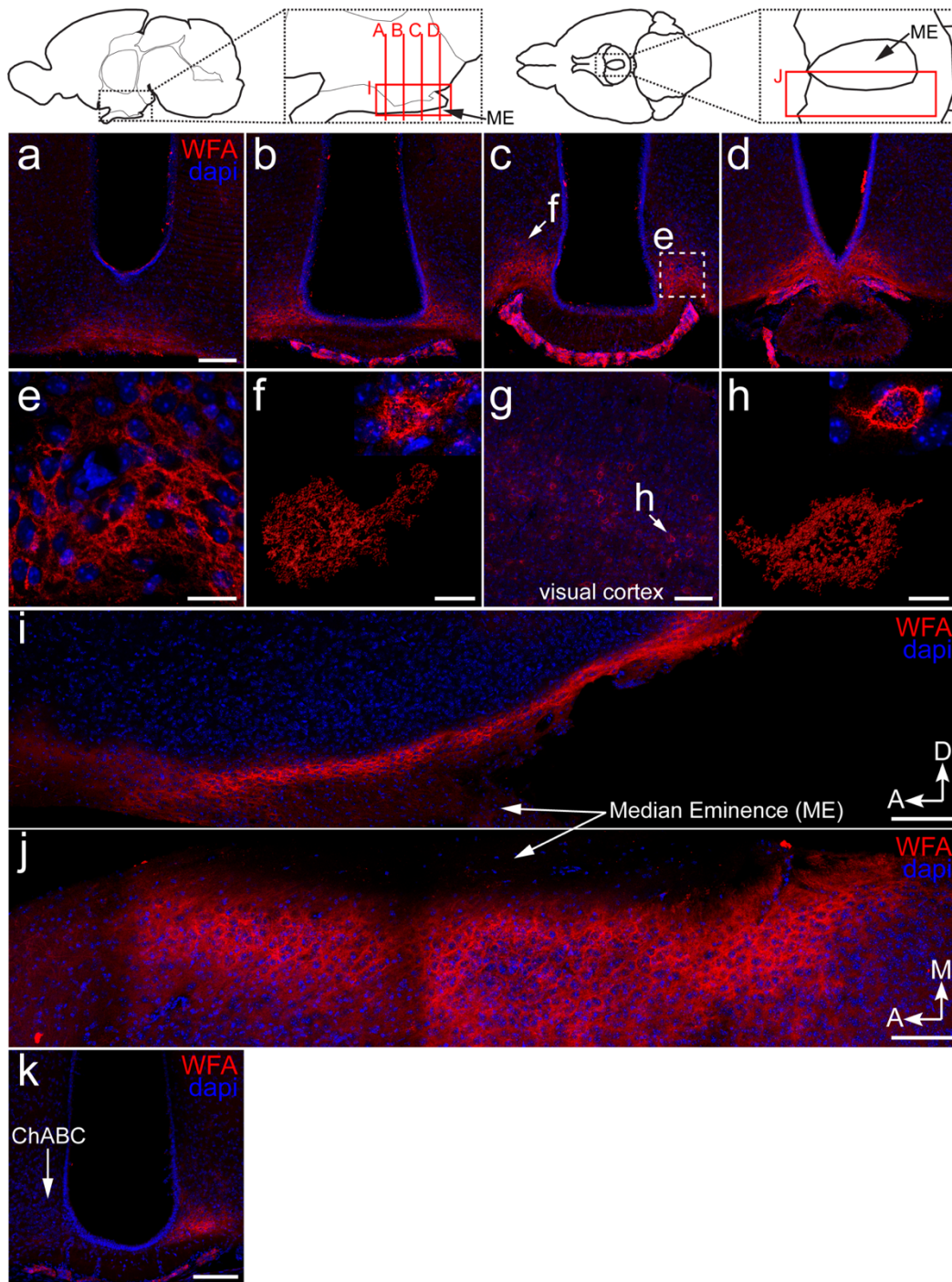


Figure 1. *Wisteria Floribunda* agglutinin (WFA)-labeling in the ventromedial ARC forms a “collar” around the ME. Diagrams at top show mid-sagittal view (left) and ventral view (right) of the mouse brain with insets showing the location and orientation of panel images. (a-d) WFA-labeled (red) coronal sections through the Arc, starting just rostral to and progressing through the ME, show a concentration of WFA-labeled cells located in the ARC at its junction with the ME. Note that the very intense staining below the ME does not correspond to labeling around neurons, but to the pia around the ME. (e) Higher magnification image of the boxed region in (c) showing the dense cluster of WFA-labeled ARC cells. (f) High magnification Imaris 3-dimensional rendering of an isolated WFA-labeled cell at the periphery of the dense cluster (arrow in c) reveals that WFA labels the soma and proximal processes of ARC cells. Inset shows the raw image. (g-h) Low (g) and high (h) magnification images of PNNs labeled by WFA in the visual cortex, where they have been extensively studied, for comparison. Note similar PNN pattern between (h) and (f) wrapping the soma and proximal process. (i-j) WFA-labeled wholemounts of the ARC viewed from the 3rd ventricle wall en-face (i) or the ventral brain surface (j) reveal the distribution of labeled ARC cells forming a “collar” around the ME, which does not contain labeling. From the ventricular surface view (i), the WFA-labeled ARC cells appear as a continuous band along the ventral margin of the ARC. (k) WFA-labeled coronal section from a wild-type mouse sacrificed 2 days after stereotactic unilateral intra-Arc injection of Chondroitinase ABC, an enzyme that digests chondroitin sulfate carbohydrates. Scale bars: 100 μ m (a-d, g, i-k), 20 μ m (e), 10 μ m (f, h). Images are representative of data from at least 5 animals.

143 As a first step to determine if these ARC WFA-labeled structures are *bone fide*
 144 PNNs, we micro-injected 10 milliunits of Chondroitinase ABC (ChABC), an enzyme that
 145 digests PNNs, stereotactically into the ARC of wild-type mice. Subsequent
 146 histochemical analysis of
 147 these animals (n=3) revealed
 148 ChABC-mediated digestion
 149 of ARC-ME PNNs on the
 150 injected side (**Fig 1k**). Then,
 151 following a previously
 152 validated protocol²⁸, we
 153 performed pre-embedding
 154 WFA-DAB labeling of mouse
 155 brain sections for study by
 156 electron microscopy. This
 157 ultrastructural analysis
 158 revealed DAB electron-dense
 159 deposits surrounding the
 160 soma (**Fig 2b** white
 161 arrowheads) and neurites
 162 (**Fig 2b** white arrows) of ARC

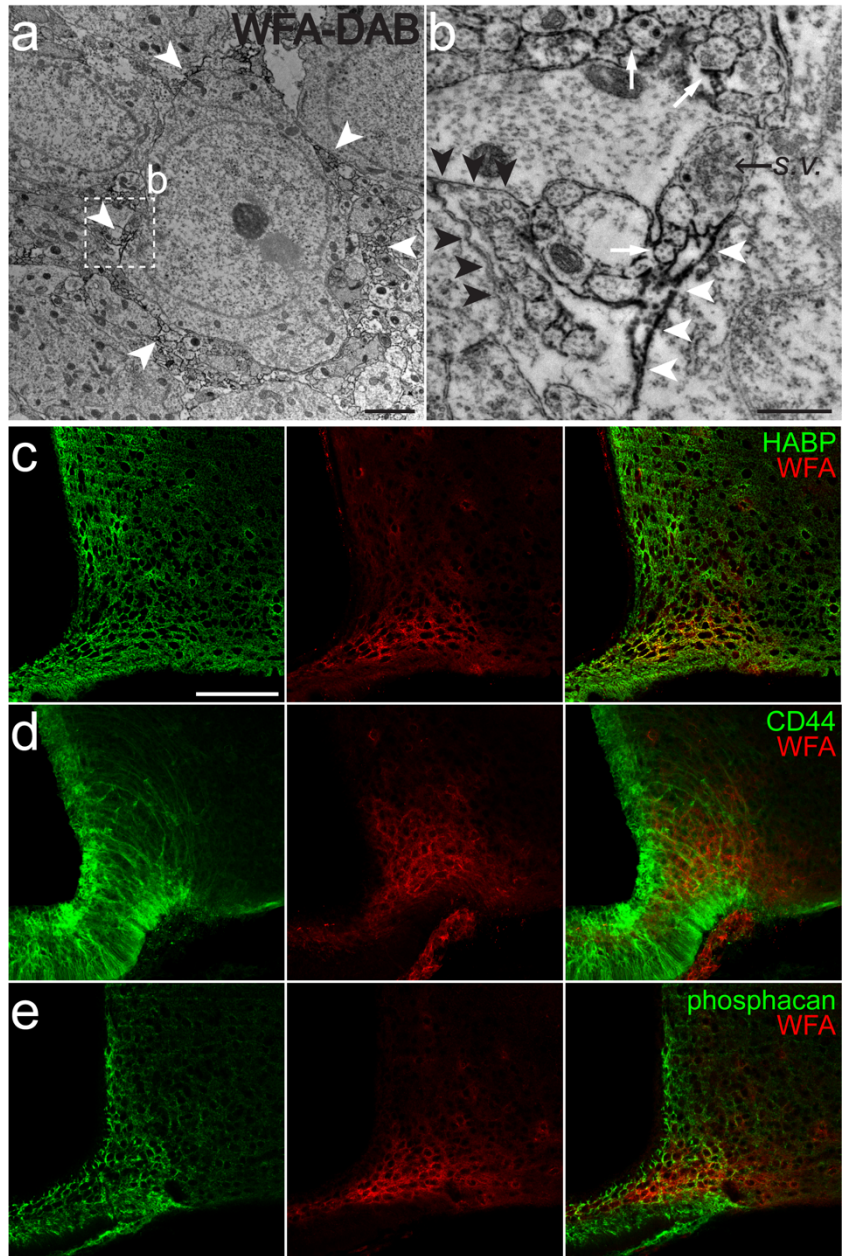
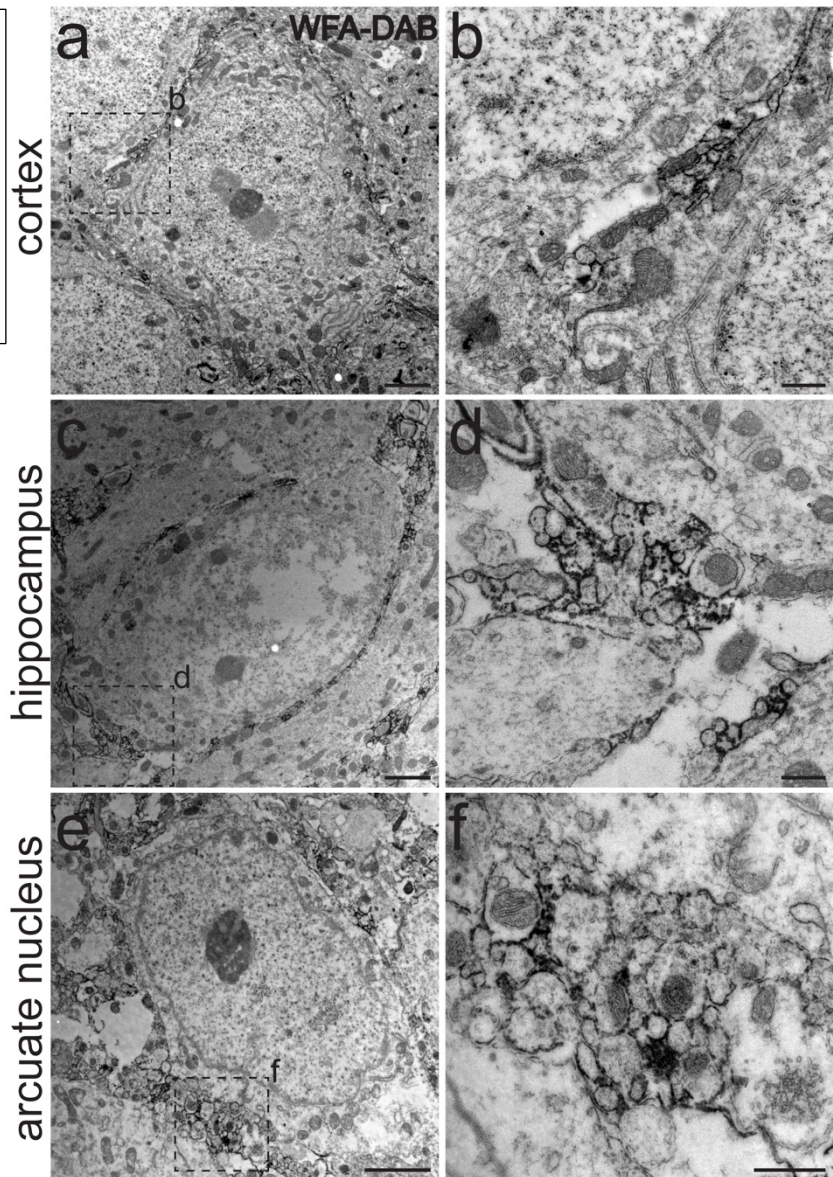


Figure 2. WFA-labelling in the ARC is observed around neuronal soma and neurites by electron microscopy and colocalizes with other major PNN components.
 (a) Low-power electron micrograph of an ARC section labeled with WFA-DAB shows electron dense DAB deposits surrounding a single ARC neuron (white arrowheads).
 (b) High-power electron micrograph corresponding to the boxed region in (a) shows WFA-labeling localized to the membrane around the cell soma (white arrowheads) and neurites (white arrows). Note labeling adjacent to an apparent terminal filled with synaptic vesicles (s.v.), as well as the appearance of non-labeled membranes (black arrowheads).
 (c-e) Confocal images of coronal sections through the ARC stained for other PNN components, including hyaluronic acid using HABP (c, green), the cell surface receptor for hyaluronic acid, CD44 (d, green), and the chondroitin sulfate proteoglycan phosphacan (e, green), show colocalization with WFA (red) in the ARC, providing evidence that ARC WFA-labeling corresponds to PNNs.
 Scale bars: 2 μ m (a), 500 nm (b), 100 μ m (c-e). Images are representative of data from at least 3 animals.

Supplementary Figure 2. Low- (a,c,e) and high-power (b,d,f correspond to boxed regions in low-power images) electron micrographs showing comparative ultrastructural distribution of WFA-DAB deposits around neurons in the cortex (a,b), hippocampus (c,d), and ARC (e,f) reveal very similar patterns of labeling localized to the soma and adjacent neurites in all 3 regions. Scale bars: 2 μ m (a,c,e), 500 nm (b,d,f). Images are representative of data from at least 3 animals.



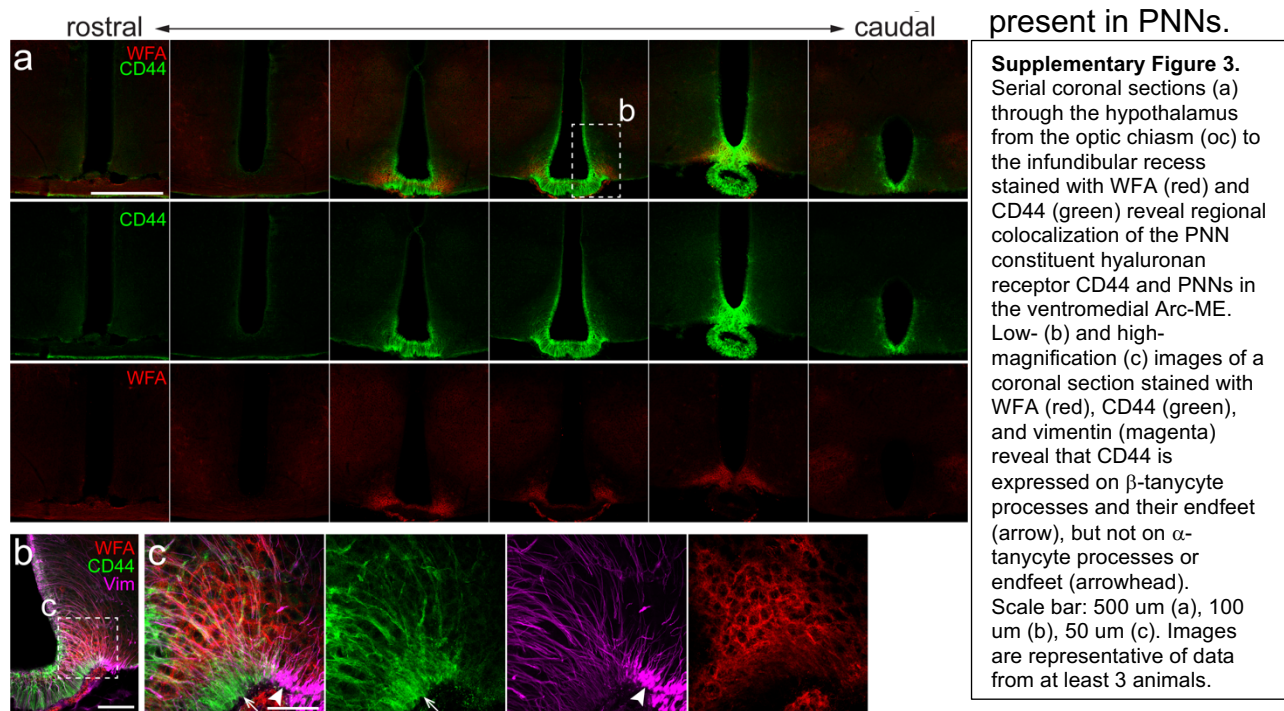
163 neurons in a distribution
 164 that closely matches the
 165 pattern observed in PNN-
 166 enmeshed cells in the
 167 cortex and hippocampus
 168 (**Supplementary Fig 2**).

169 In addition to
 170 chondroitin sulfate (CS)
 171 carbohydrate chains labeled
 172 by WFA, PNNs are
 173 comprised of two other
 174 major components: the CS

175 proteoglycan (CSPG) core proteins to which the CS chains covalently bind, and
 176 hyaluronic acid (HA), a long carbohydrate polymer to which CSPG core proteins
 177 noncovalently bind. Using biotinylated-HA-binding protein (HABP)²⁹, we histochemically
 178 stained HA in the hypothalamus. Although HABP lightly stains the extracellular matrix
 179 throughout brain parenchyma, we observed an increased abundance of HA that
 180 colocalizes with WFA at the junction of the ARC and ME (**Fig 2c**), confirming that WFA
 181 (+) structures in this brain area contain HA. To identify the relevant CSPG(s) present in

182 these PNNs, we next stained for each of the 5 major CSPG species found in PNNs
 183 elsewhere in the brain: aggrecan, brevican, neurocan, versican and phosphacan.
 184 Interestingly, although each of these CSPGs was detected in various mouse brain areas
 185 (data not shown), only phosphacan immunoreactivity was co-localized with WFA in
 186 mouse ARC-ME (**Fig 2e**).

187 We also immunostained for CD44, the cell surface receptor for HA, and found
 188 that its expression in this brain area is largely limited to tanycytes, with high expression
 189 localized to E3/ β -tanycytes piercing through the PNN domain (**Fig 2d**) and little to no
 190 expression in dorsal E2/ α -tanycytes that circumvented the PNN domain
 191 (**Supplementary Fig 3b, c**). An IHC survey of CD44 expression in serial coronal
 192 sections through the hypothalamus revealed a striking colocalization with the PNN
 193 domain in the ventromedial ARC (**Supplementary Fig 3a**). These findings raise the
 194 possibility that via activation of CD44, signal transduction in tanycytes is evoked by HA



196

197 The ARC is uniquely specialized to sense and transduce input from nutritionally-
198 relevant hormones (such as leptin and insulin) and nutrients (*e.g.*, glucose, free fatty
199 acids and amino acids) into adaptive changes of food intake and energy metabolism³⁰.
200 Among key neuronal subsets implicated in this homeostatic circuitry are *Agrp* and pro-
201 opiomelanocortin (*Pomc*) neurons, with the former being GABAergic³¹. To identify
202 distinct ARC neuronal subtypes that are among those enmeshed by PNNs (= # neurons
203 of particular subtype / total # PNN-enmeshed cells), we performed IHC on coronal
204 sections from transgenic mouse lines that provided whole cell GFP-filling. Using
205 GAD67-GFP heterozygous knock-in mice¹, we confirmed that a vast majority of ARC
206 neurons enmeshed by PNNs are GABAergic ($81.8 \pm 0.7\%$ of ARC PNN-enmeshed
207 cells; $n=3$ GAD67-GFP mice; note that dots in dot plots throughout this work represent
208 data from independent animals) (**Fig 3a-d**), as is the case for PNN-enmeshed neurons
209 in other brain areas^{10,17}. Three-dimensional reconstruction of GAD67-GFP+ PNN-
210 enmeshed cells (**Supplementary Movie 1**) revealed PNN enmeshing the soma and
211 proximal dendrites of GABAergic ARC cells in a manner comparable to that of
212 GABAergic interneurons in V1, with some differences in morphology due likely to
213 differences in cell type and process ramification (**Supplementary Fig 4** and
214 **Supplementary Movie 2**).

215 To determine if ARC neurons that express leptin receptors are represented
216 among those enmeshed by PNNs, we employed Leptin Receptor b-Cre;Ai14 td-Tomato
217 reporter mice to histochemically identify leptin-receptor positive cells. These cells
218 comprised $81.7 \pm 1.5\%$ of all PNN-enmeshed cells in the ARC ($n=3$ LepRb-Cre;Ai14)
219 (**Fig 3e-g**). To identify *Agrp* neurons, we used NPY-GFP transgenic mice (since NPY

220 and *Agrp* are expressed in the same ARC neuronal subset) and found that these cells
 221 (which are GABAergic, and many of which express leptin receptors) also account for a
 222 majority of ARC PNN cells ($58.5 \pm 1.0\%$; $n=3$ NPY-GFP mice) (**Fig 3h-j** and
 223 **Supplementary Movie 3**). By comparison, POMC neurons comprised a much smaller
 224 fraction of PNN-enmeshed cells in this brain area ($13.7 \pm 2.3\%$; $n=3$
 225 POMC-GFP mice) (**Fig 3k-m**).

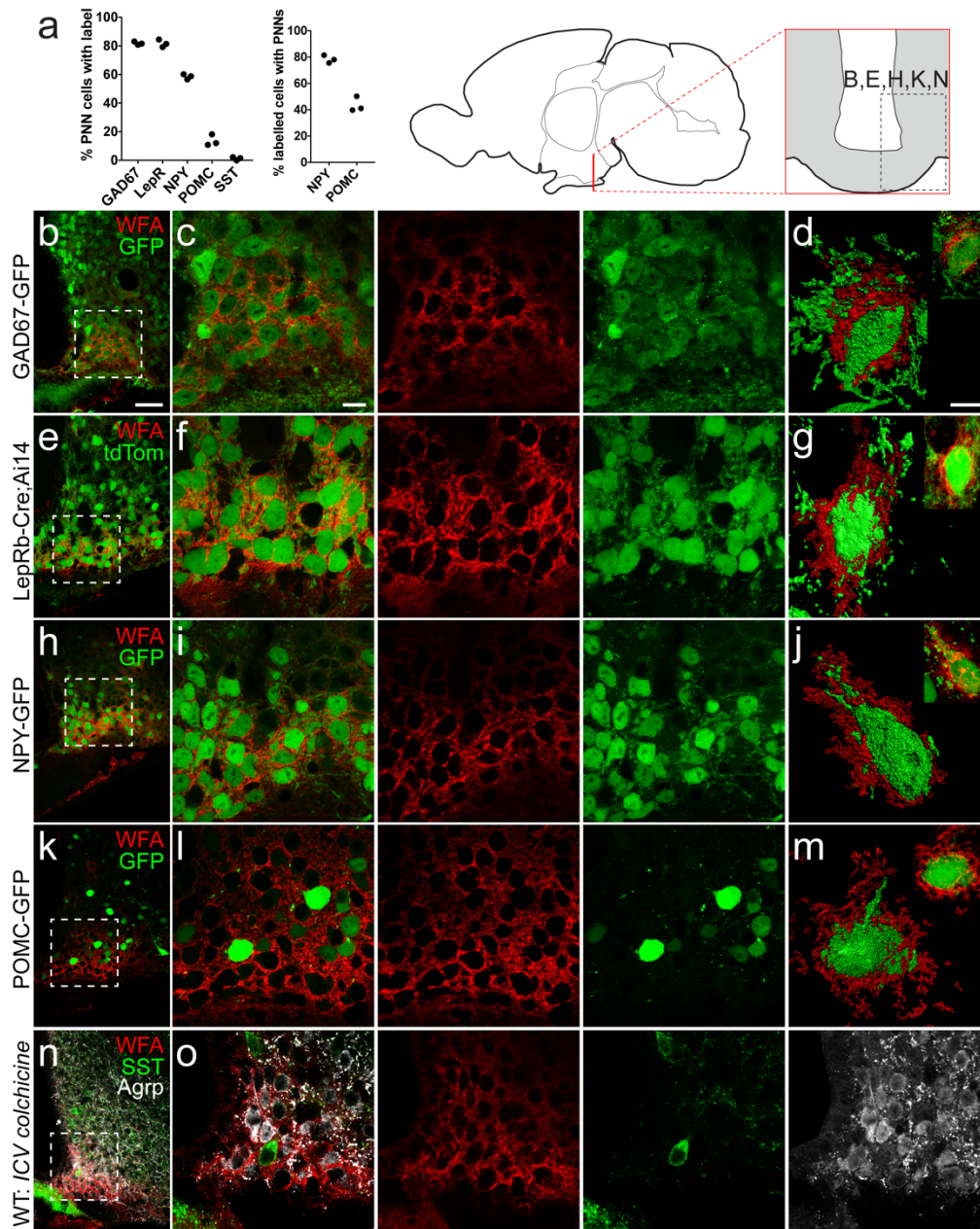
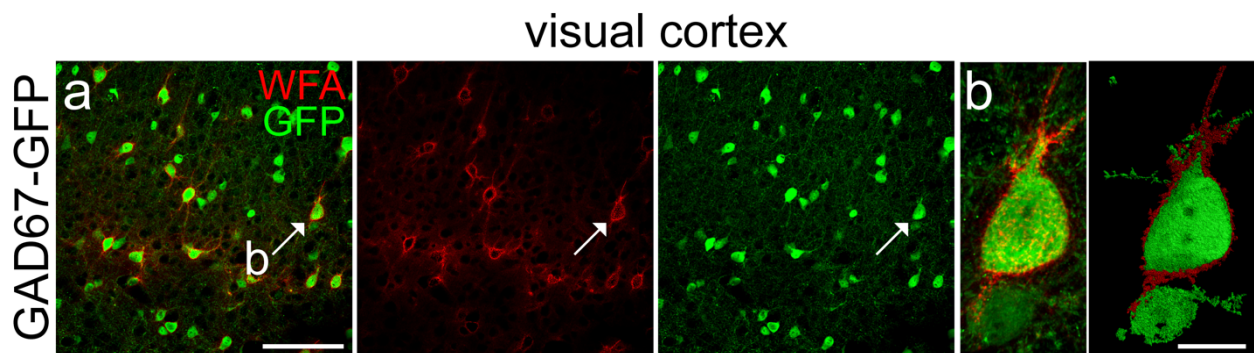


Figure 3. PNNs enmesh GABAergic, LepRb-positive, Agrp/NPY neurons in the Arc. Diagram at top shows mid-sagittal view of mouse brain with location and orientation of panel images. (a) Dot plots show the proportion of individual neuronal subtypes enmeshed by PNNs. Dots in this and all subsequent dot plots represent data from independent animals. The left plot shows the percentage of all PNN-enmeshed ARC cells that belong to a particular neuronal subtype. The right plot shows the percentage of all ARC Npy-GFP or POMC-GFP cells that are enmeshed by PNNs. Low (b, e, h, k, n) and high (c, f, i, l, o) magnification images of coronal sections stained with WFA (red) and antibodies to GFP (green) (b, h, k), dsRed (green) (e), or SST (green) and Agrp (white) (n) show that most PNN-enmeshed cells are GAD67-GFP-positive (GABAergic), LepRb-positive, and NPY-positive, while few enmeshed cells express POMC or SST. (d, g, j, m) High magnification Imaris 3-dimensional surface rendering of isolated ARC PNN-enmeshed cells belonging to the various neuronal subtypes (corresponding to b, e, h, k, respectively) show PNNs wrapping the soma and proximal processes. Insets show raw images. See corresponding supplementary movies 1 and 3 for (d) and (j), respectively. Scale bars: 50 μ m (b, e, h, k, n), 20 μ m (c, f, i, l, o), 10

226 A separate but related question pertains to the fraction of Agrp or POMC neurons
227 in the ARC that are enmeshed by PNNs (= # PNN-enmeshed neurons of particular
228 subtype / total # neurons of that subtype). As predicted, the fraction of Agrp neurons
229 enmeshed by PNNs (78.3 ± 1.7% NPY-GFP neurons) is greater than the fraction of
230 POMC neurons (43.6 ± 3.3% POMC-GFP neurons). A third peptidergic cell type found
231 in the ARC expresses somatostatin (SST), which is challenging to detect
232 histochemically because the SST peptide is rapidly exported from soma into axons. To
233 address this issue, we administered a single intracerebroventricular (ICV) injection of
234 colchicine to wild-type mice, which prevents transport of SST out of the soma and thus
235 enables somatic labeling with SST antibodies. We report that while this approach
236 allowed us to identify ample SST+ soma, few of these were PNN-enmeshed (1.2 ±
237 0.6%; n=3) (**Fig 3n-o**). As confirmation of the efficacy of ICV colchicine to prevent
238 neuropeptide export from the soma, we note that many Agrp+ PNN-enmeshed cell
239 bodies were also observed, corroborating our findings in NPY-GFP mice (**Fig 3o**).
240 Together, these findings indicate that only a subset of ARC neurons – specifically, those
241 neurons most closely linked to control of energy balance and metabolic homeostasis –
242 are enmeshed by PNNs.

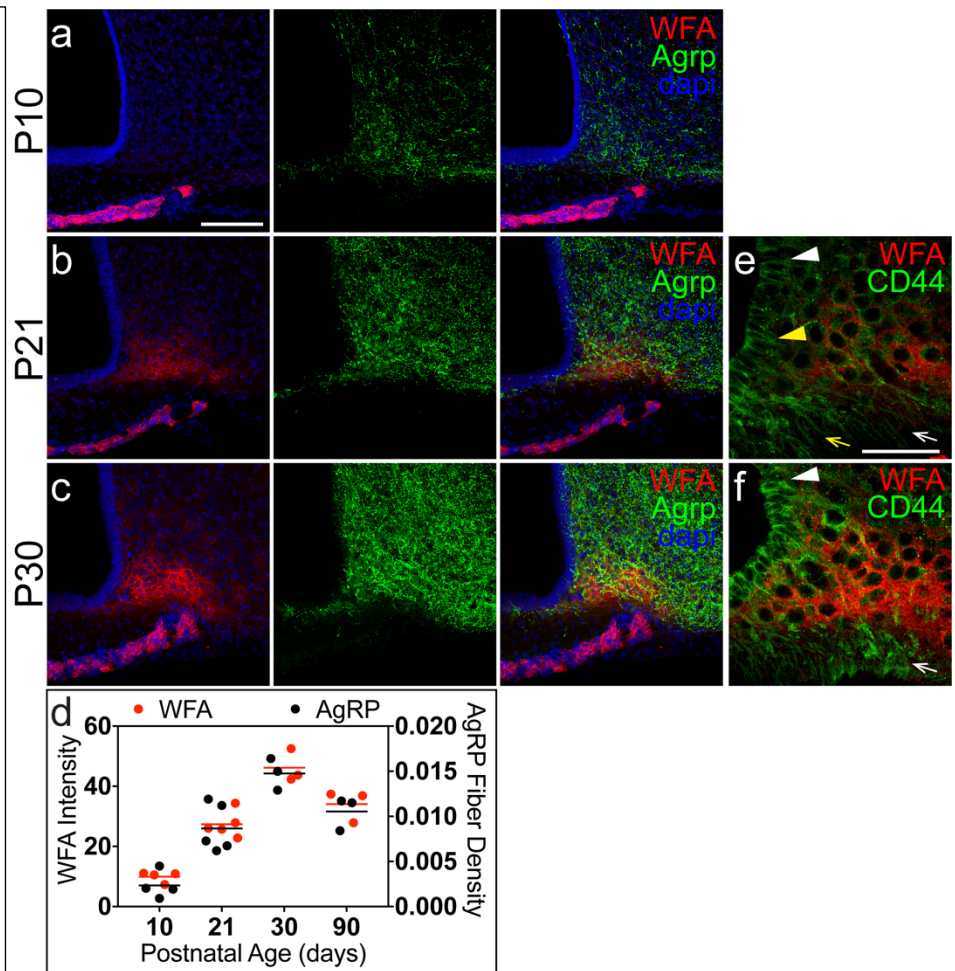


Supplementary Figure 4. PNNs enmesh GABAergic interneurons in the visual cortex.
(a) Confocal image of a coronal section through the primary visual cortex of a GAD67-GFP mouse stained with WFA (red) and GFP antibody (green) shows many PNN enmeshed GABAergic interneurons in layer II-III. Arrow indicates cell shown in (b).
(b) High magnification confocal image (left) and Imaris 3-dimensional surface rendering (right) of an isolated PNN-enmeshed GABAergic interneuron shows PNNs wrapping the soma and proximal processes. Scale bars: 100 um (a), 20 um (b). Images are representative of data from at least 5 animals.

243 A key question raised by these observations is whether PNNs contribute to
244 closure of the CP for ARC neurocircuit development, as is true of V1 and other brain
245 areas. As a first step to address this question, we performed a developmental time-
246 series analysis of PNN formation over the lactation and periweaning period from
247 postnatal day 10 (P10) to P30 in wildtype mice (**Fig 4**). This approach was based on
248 evidence that leptin-dependent maturation of ARC-ME neurocircuits occurs during a CP
249 that closes \sim P28^{18,19,21}, so PNNs must appear during this period if they are to contribute
250 to closure of this CP. WFA labeling revealed only a very faint signal at P10 (10.0 ± 0.8
251 intensity units; n=4 C57B/6 mice) that lacked the typical PNN honeycomb configuration
252 (**Fig 4a**). By P21, WFA labeling intensity had increased by more than 2-fold (27.4 ± 1.7
253 intensity units; n=5 mice) and structural features of PNNs were evident (**Fig 4b**). WFA
254 intensity was further increased at P30 (46.2 ± 2.6 intensity units; n=3 mice), by which
255 time PNN structures appeared fully formed (**Fig 4c**).

256 The time course of ARC PNN formation during postnatal development in wildtype
257 mice was closely paralleled by the maturation of Agrp neuron projections, quantified as
258 an increase in Agrp fiber density in the ARC ($0.23 \pm 0.07\%$ at P10; $0.87 \pm 0.11\%$ at P21;
259 $1.48 \pm 0.14\%$ at P30) (**Fig 4d**). We note that at CP closure (\sim P28), both PNNs and
260 Agrp fiber density in the ARC were transiently increased over values characteristic of
261 adult mice (P90: WFA 34.1 ± 2.5 intensity units; Agrp fiber density $1.05 \pm 0.09\%$).
262 During postnatal development, the domain of CD44 expressing tanycytes also
263 expanded from medial (where it covered only the ME β -tanycytes at P21) to lateral and
264 dorsal along the ventricular lining, paralleling the progressive appearance of PNNs (**Fig**
265 **4e,f**; compare yellow and white arrows and arrowheads).

Figure 4. PNN formation in the ARC occurs during the lactation and periweaning period, corresponding with the maturation of *Agrp* neurons. (a-c) Confocal images of coronal sections stained with WFA (red), *Agrp* (green), and dapi (blue) from postnatal wild-type mice at age P10 (a), P21 (b), and P30 (c). PNN staining intensity and ARC *Agrp* fiber density increase in parallel over this time period. (d) Dot plot shows correlated increase in WFA intensity and *Agrp* fiber density in the ARC from P10 to P30, as well at P90. Dots (WFA intensity in red, *Agrp* density in black) represent values from individual animals and horizontal bars represent the mean. WFA intensity is represented by the average over all voxels in the ARC region of interest, with range 0-255. *Agrp* fiber density is measured as the volume of *Agrp*+ voxels divided by the total volume of the ARC region of interest. (e, f) High magnification confocal images of coronal sections stained with WFA (red) and CD44 (green) show that CD44 expression in tanyocyte processes and endfeet extends from (e) more medial ME β -tanyocytes at P21 (yellow arrowhead indicates cell bodies and yellow arrow indicates endfeet) to (f) more laterally located β -tanyocytes with processes penetrating the ARC at P30 (white arrowhead and arrow), concomitant with the increase in PNN intensity over the same period. Scale bars: 100 μ m (a-c), 50 μ m (e, f). Images are representative of data from at least 3 animals.



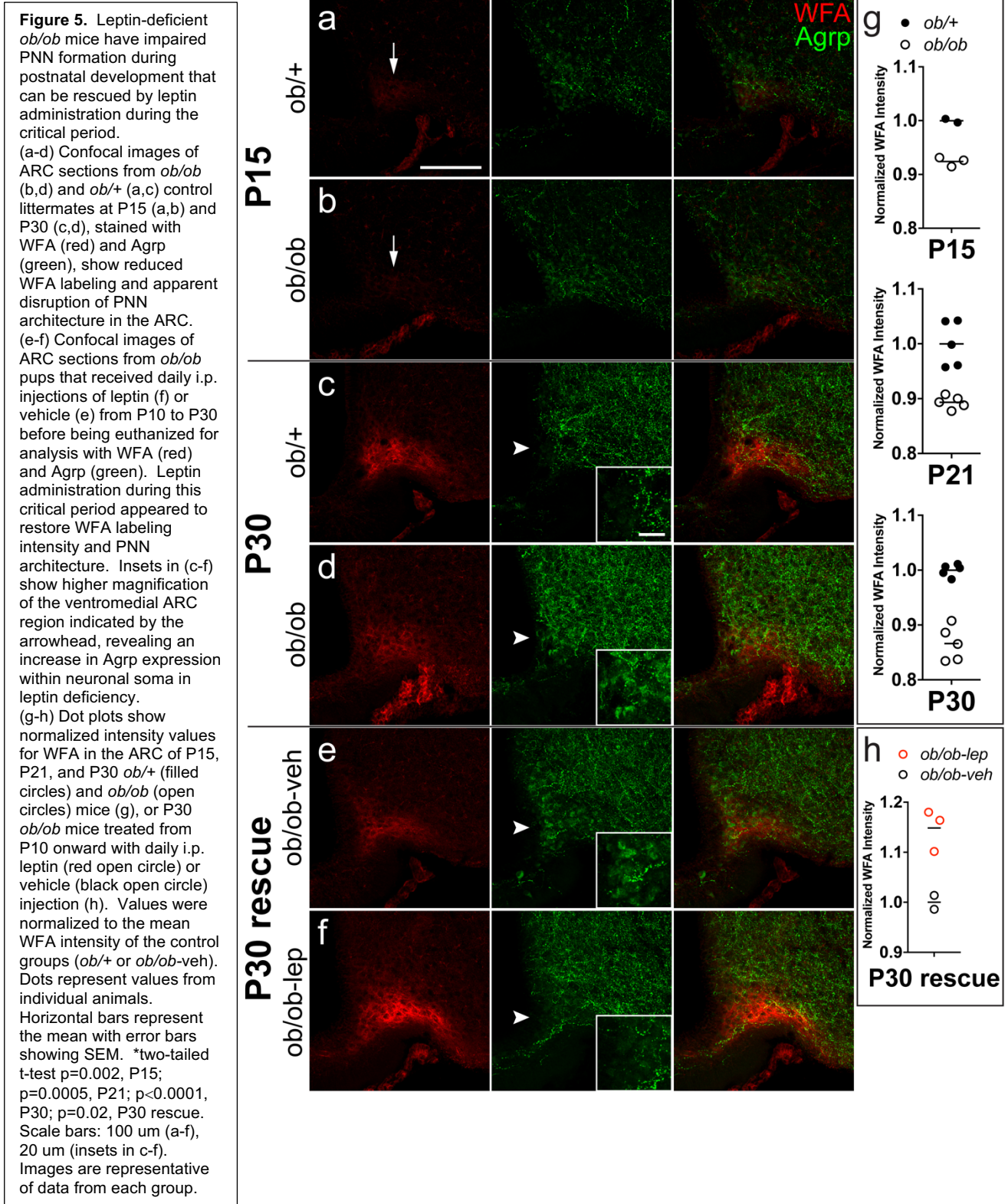
The tight temporal association between ARC PNN

267 formation and maturation of *Agrp* neuron projections

268 coincides closely with closure of the CP for *Agrp* neuron development (\sim P28)¹⁸. Given
 269 the key role played by leptin in the latter process, we next sought to investigate whether
 270 input from leptin influences ARC PNN formation. To this end, we performed a
 271 developmental time-series analysis of ARC WFA labeling in *ob/ob* pups and *ob/+*
 272 control littermates at P15, P21, and P30. At each of these ages, we found that in *ob/ob*
 273 mice, ARC WFA intensity (normalized to the mean value of control littermates) was
 274 significantly below that detected in controls (P15: 0.92 ± 0.01 , $n=3$ *ob/ob* vs. $1.00 \pm$
 275 0.00 , $n=2$ *ob/+*, $p=0.002$; P21: 0.89 ± 0.01 , $n=5$ *ob/ob* vs. 1.00 ± 0.02 , $n=5$ *ob/+*,

276 $p=0.0005$; $P30$: 0.87 ± 0.01 , $n=5$ *ob/ob* vs. 1.00 ± 0.00 , $n=5$ *ob/+*, $p<0.0001$) (Fig 5a-d,

277 g).



279 Based on these results, we hypothesized that like *Agrp* neuron maturation,
280 formation of PNNs in the ARC is dependent on input from circulating leptin. To test this
281 hypothesis, we administered either leptin or vehicle to *ob/ob* pups according to a
282 schedule reported to mimic the postnatal leptin surge that was used to define the CP for
283 *Agrp* neuron maturation¹⁸. Specifically, *ob/ob* pups received a daily intraperitoneal
284 injection of either leptin (10 mg/kg) or vehicle from P10 to P30, and were euthanized
285 one day later for IHC analysis. As predicted, ARC WFA intensity was significantly
286 increased in leptin-compared to vehicle-treated *ob/ob* pups (*P30 rescue*: 1.15 ± 0.02 ,
287 $n=3$ *ob/ob-leptin* vs. 1.00 ± 0.01 , $n=2$ *ob/ob-vehicle*, $p=0.02$) (**Fig 5e, f, h**). There was
288 no significant difference in weight gain between the leptin and vehicle-treated groups.
289 Interestingly, the presence of *Agrp*⁺ soma in the ARC of vehicle-treated pups, but not
290 leptin-treated pups (insets in **Fig 5e, f**) appears to offer confirmatory evidence of leptin
291 action, which is known to reduce *Agrp* expression³². A similar pattern was also
292 observed when *Agrp* staining between *ob/+* and *ob/ob* pups was compared at P30
293 (insets in **Fig 5c, d**).

294 To determine how ARC PNNs are affected by persistent leptin deficiency in
295 adulthood, we performed WFA labeling of 12 week-old *ob/ob* mice and age-matched
296 C57B/6 mice followed by high-resolution confocal microscopy and Imaris 3-dimensional
297 image analysis (**Fig 6a, b**). Paradoxically, in the ARC-ME area, WFA intensity in *ob/ob*
298 mice (normalized to the mean value of age-matched controls) was significantly higher
299 than in controls (1.24 ± 0.05 , $n=5$ *ob/ob* vs. 1.00 ± 0.03 , $n=5$ wt; $p=0.004$)(**Fig 6e**),
300 whereas no such difference in intensity was detected in primary visual cortex of the
301 same animals (1.00 ± 0.01 , $n=5$ *ob/ob* vs. 0.99 ± 0.01 , $n=5$ wt; $p=0.2$) (**Supplementary**

302 **Fig 5).** To investigate whether this increase of ARC PNN density in *ob/ob* mice was the
 303 result of leptin deficiency or
 304 was instead secondary to
 305 obesity, we compared WFA
 306 staining intensity between
 307 cohorts of wild-type C57B/6
 308 mice that were either made
 309 obese through high-fat diet
 310 (HFD) feeding for 12 weeks
 311 (beginning at age 12 weeks)
 312 or were fed standard chow
 313 and sacrificed at the same
 314 age. We report that
 315 whereas no difference in
 316 ARC WFA intensity was
 317 detected between HFD and
 318 chow-fed cohorts
 319 (1.00 ± 0.00 , $n=5$ hfd vs.
 320 1.00 ± 0.00 , $n=3$ chow),
 321 tanycytic CD44 expression
 322 was increased in the former
 323 group (1.11 ± 0.03 , $n=5$ hfd vs.
 324 1.00 ± 0.01 , $n=5$ chow);

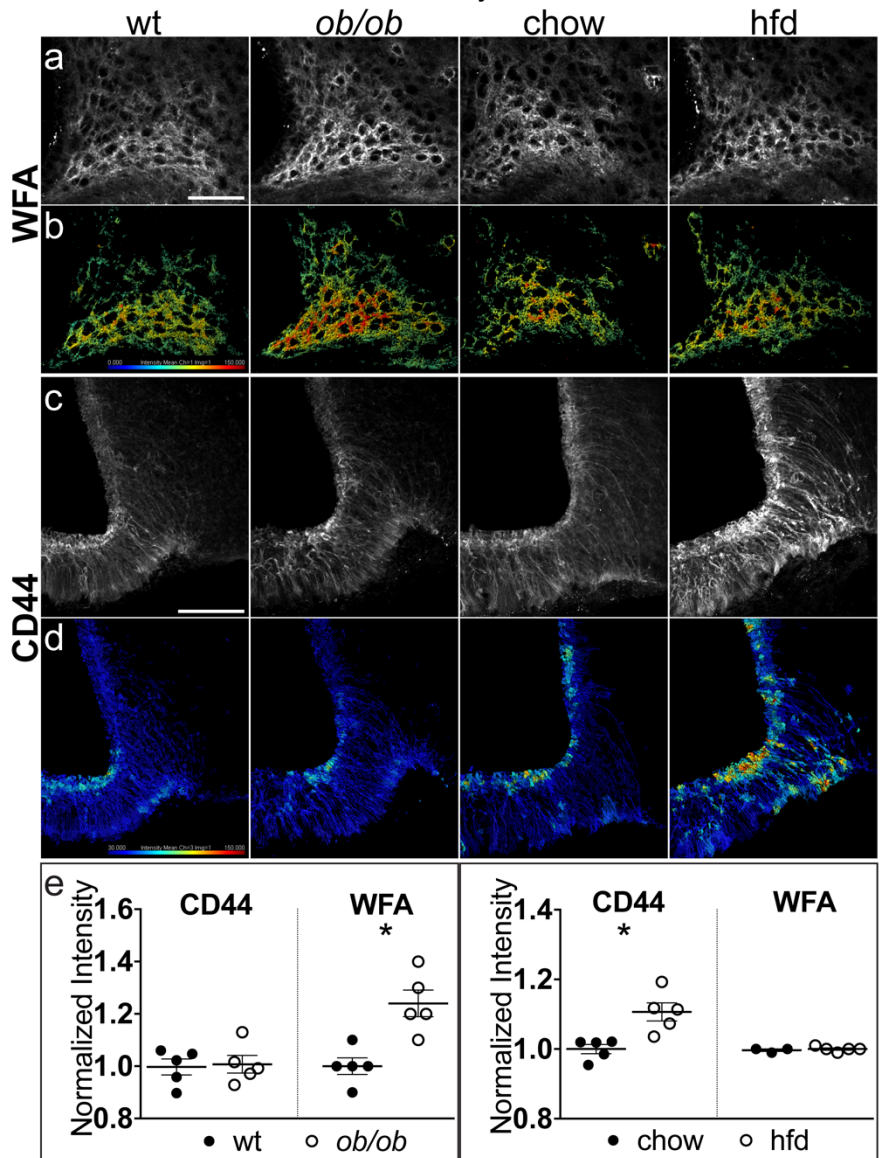
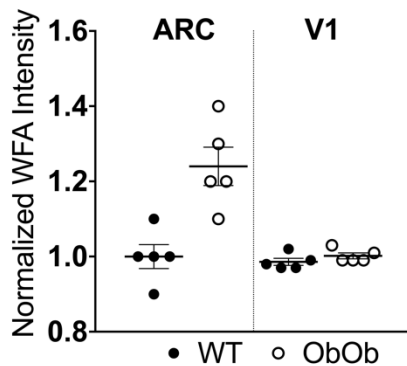


Figure 6. Leptin-deficient *ob/ob* mice and DIO mice fed a high fat diet, two rodent models of obesity and glucose intolerance, exhibit altered ARC PNNs or PNN constituents. (a, b) High magnification confocal images (a) of coronal sections stained with WFA and corresponding Imaris spectral images (b) showing voxel intensity from C57B/6 wt, *obob*, chow-fed, or high-fat diet (HFD) -fed mice. Adult *obob* mice exhibited increased ARC PNN intensity compared to wt, but there was no difference between mice fed chow and HFD. (c, d) High magnification confocal images (c) of coronal sections stained with CD44 and corresponding Imaris spectral images (d) showing voxel intensity from C57B/6 wt, *obob*, chow fed, or HFD fed mice. DIO mice fed HFD exhibited increased tanycyte CD44 expression compared with chow fed mice, with no difference observed between wt and *obob* mice. Note that wt and *obob* mice are age-matched 3 mo old mice fed standard chow diet. Chow and HFD mice were C57B/6 wt mice that were fed either chow or hfd for 12 weeks (beginning at age 3 mo. and sacrificed at age 6 mo.). Spectral reference line shown in (b) with intensity range 0 to 150 and (d) with range 30 to 150. (e) Dot plots show normalized intensity values for CD44 and WFA in the ARC of wt and *obob* mice (left) and chow and HFD mice (right). Values were normalized to the mean WFA or CD44 intensity of the control groups (wt or chow). Dots represent values from individual animals. Horizontal bars represent the mean with error bars showing SEM. *two-tailed t-test $p=0.004$ for WFA *obob* v. wt, $p=0.007$ for CD44 HFD v. chow. Scale bars: 50 μ m (a), 100 μ m (c). Images are representative of data from each group.

325 p=0.007)(Fig 6c-e). In contrast, no difference in tanycytic CD44 expression was
 326 observed between *ob/ob* and chow-fed control mice (1.01 ± 0.03 , $n=5$ *ob/ob* vs.
 327 1.00 ± 0.03 , $n=5$ wt; $p=0.8$). Together, these data suggest that increased PNN density in
 328 the ARC of adult *ob/ob* mice is secondary to leptin deficiency rather than to obesity *per*
 329 *se*, whereas the reverse is true for the increase of tanycytic CD44 expression in HFD-
 330 fed (but not *ob/ob*) mice.



Supplementary Figure 5. Dot plot shows normalized intensity values for WFA in the ARC and V1 of wt and *ob/ob* mice. Increased WFA intensity in *ob/ob* mice was seen in the Arc, but not in V1. Values were normalized to the mean WFA intensity of wt ARC or V1. Dots represent values from individual animals. Horizontal bars represent the mean with error bars showing SEM.

To determine if PNNs are present in the ARC of other mammalian species, we performed WFA staining in the hypothalamus of both rats and humans. We report that PNNs are present in the ARC-ME of all 3 species (Supplementary Fig 6). As in the mouse, a majority of cells enmeshed by PNNs in the human ARC are NPY/Agrp neurons, with both the soma and proximal dendrites of these neurons wrapped by WFA+ material (Fig 7 and Supplementary Movie 4). Interestingly,

340 PNN-enmeshed cells in humans are more sparsely distributed than those in mice, which
 341 enhances the ability to see how the mesh structure associates with the neuronal
 342 contours.

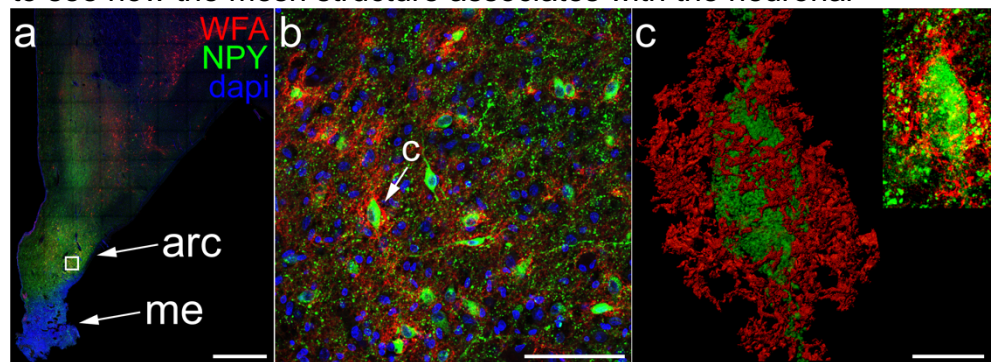
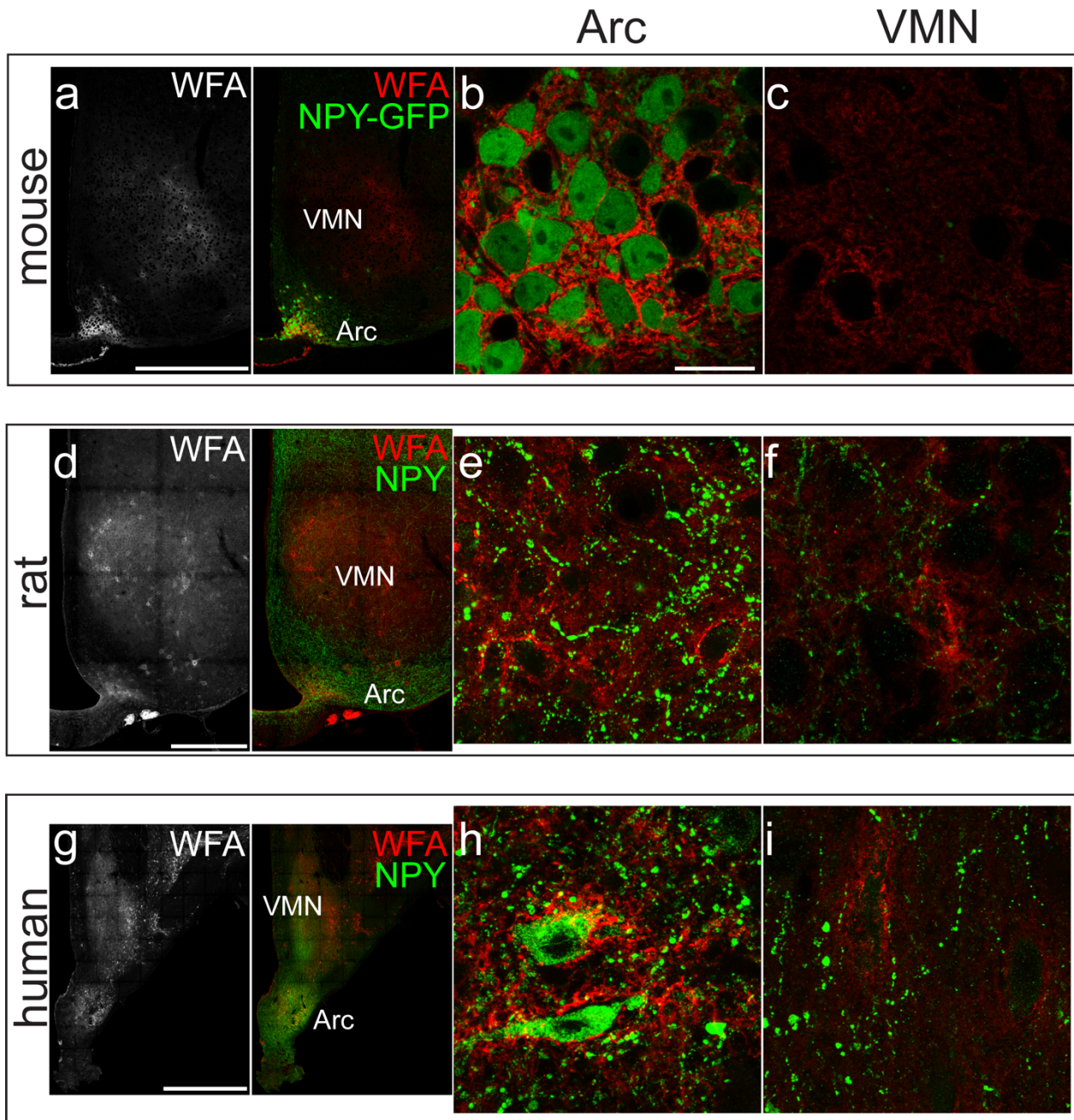


Figure 7. PNNs enmesh NPY+ neurons in the human Arc. (a) Multi-tile confocal image of a coronal section through the human mediobasal hypothalamus stained with WFA (red), NPY (green), and dapi (blue). Boxed region shows location of image in (b). (b) High magnification image shows many PNN-enmeshed NPY+ cells in the human Arc. Arrow indicates cell shown in (c). (c) High magnification Imaris 3-dimensional surface rendering of human ARC PNN-enmeshed NPY+ cell shows PNNs wrapping the soma and proximal processes, as in the mouse ARC and PNN-enmeshed cells in other brain areas. Inset shows raw image with WFA (red) and NPY (green). See corresponding supplementary movie 4. Scale bars: 2 mm (a), 100 μ m (b), 10 μ m (c). Images are representative of data from 2 human specimens.



Supplementary Figure 6. PNNs are conserved across the mouse, rat, and human Arc. (a, d, g) Low magnification confocal images of coronal sections from mouse (a), rat (d), and human (g), stained with WFA and GFP (Npy-GFP mice in (a)) or NPY (d, g). Across species, the ARC displays more intense WFA-labeling than the nearby VMN, where WFA labeling is diffuse. This is confirmed in higher magnification confocal images of the ARC (b, e, h) and VMN (c, f, i). Scale bars: 500 μ m (a, d), 20 μ m (b, c, e, f, h, i), 4 mm (g).

345 Discussion

346 We report that PNNs enmesh *Agrp* and other leptin receptor-expressing neurons
 347 in the ARC (most of which are GABAergic, similar to neurons enmeshed by PNNs in

348 visual cortex and other brain areas), and that their appearance during postnatal
349 development coincides closely with both maturation of *Agrp* neuron projections and
350 closure of the CP for leptin-mediated regulation of *Agrp* neuron development¹⁸.
351 Situated at the junction of the ARC and ME, these PNNs are detected in humans as
352 well as rodents, and their formation appears to be sensitive to input from leptin, being
353 deficient in the ARC of postnatal *ob/ob* mice, and restored by leptin administration to
354 *ob/ob* mice during the CP. Together, these findings support a model in which PNNs
355 contribute to closure of the CP for the development of neurocircuits crucial to control of
356 energy balance and glucose metabolism in adulthood, and suggest that leptin regulation
357 of ARC neuron development during the CP involves an action on PNN formation. To
358 our knowledge, these findings also offer the first demonstration of PNN formation that is
359 responsive to input from a circulating hormone.

360 In sharp contrast to the deficiency of PNNs we observed in the ARC during
361 postnatal development, adult *ob/ob* mice exhibit an overabundance of ARC PNNs. To
362 explain this paradoxical finding, we draw upon both *in vivo*^{9,33,34} and *in vitro*³⁵ evidence
363 that PNN formation is driven by activity of the enmeshed neuron. Thus, leptin induces
364 depolarization and increases the excitability of *Agrp* neurons during the CP (prior to
365 ~p21-23)²², so leptin action on these neurons may constitute a stimulus to PNN
366 formation during this time. During subsequent development, however, a progressive
367 increase in the expression of ATP-sensitive potassium channels by *Agrp* neurons leads
368 to a “phenotype switch”, whereby leptin now exerts the hyperpolarizing effect
369 characteristically observed in adult *Agrp* neurons²². Consequently, *Agrp* neuron activity

370 is predicted to be reduced in leptin-deficient mice during the CP, but increased in
371 adulthood, and PNN formation parallels these changes.

372 Available evidence suggests both that ARC neurocircuits are highly plastic during
373 development and that this plasticity is markedly reduced upon CP closure. Thus,
374 whereas *Agrp* neuron ablation induces life-threatening starvation when it occurs in adult
375 mice, it has little or no phenotypic impact when induced shortly after birth³⁶. Similarly,
376 CRISPR-mediated deletion of leptin receptors selectively from *Agrp* neurons in adults
377 recapitulates most of the phenotype of whole body leptin deficiency (hyperphagia,
378 obesity and diabetes), whereas the same deletion has little detectable effect when
379 induced during development³⁷. Combined with evidence that over the course of the CP,
380 when *Agrp* neurons innervate their downstream targets^{18,19,21}, their response to leptin
381 switches from excitatory to inhibitory²², these data collectively point to the existence of a
382 mechanism whereby *Agrp*-linked circuit plasticity during postnatal development is
383 sharply constrained in adulthood. PNNs are likely candidates to mediate this effect, as
384 they can limit plasticity both through direct signaling effects of CSPGs on the enmeshed
385 neuron and by providing a scaffold for binding regulatory molecules such as *Otx2*¹⁴
386 (which suppresses plasticity) and the chemorepulsive molecule Semaphorin 3a³⁸ (which
387 promotes growth of projections away from the enmeshed neuron)^{8-15,38}.

388 Such a role for PNNs has important implications for understanding how
389 nutritional excess during postnatal development affects ARC neurocircuits in ways that
390 can predispose to obesity and T2D in adulthood^{30,39,40}. Specifically, over-nutrition
391 during lactation, due either to maternal HFD consumption^{23,25-27} or to culled litter size²⁴,
392 1) reduces numbers of ARC neurons expressing leptin receptors. 2) decreases leptin

393 responsiveness of these neurons^{23,24}, 3) impairs formation of ARC projections within
394 hypothalamic feeding circuits^{23,25}, and 4) predisposes to excess body adiposity and
395 metabolic dysregulation in adulthood²⁵⁻²⁷. Similarly, epidemiological evidence suggests
396 that in humans, late gestation and early childhood are particularly sensitive periods
397 when environmental exposures can shape a predisposition to metabolic disease in
398 adulthood⁴¹. Interestingly, early gestational undernutrition is also reliably associated
399 with an increased risk of adult obesity⁴²⁻⁴⁴, and this effect can be partially reversed by
400 leptin treatment during the lactation period⁴⁵. Since PNNs sharply limit the plasticity of
401 neurons that they enmesh, and since elsewhere in the brain, the developmental
402 appearance of PNNs heralds CP closure¹⁷, we interpret our discovery that ARC neurons
403 become enmeshed by PNNs at a time corresponding to CP closure as being of potential
404 relevance to experience-dependent plasticity in neurocircuits for energy balance and
405 glucose homeostasis. It is possible, for example, that experimental re-activation of ARC
406 plasticity in adults will ameliorate metabolic dysfunction, as has been observed following
407 re-induction of plasticity in the visual cortex in models of amblyopia⁸.

408 In addition to limiting plasticity during development, PNNs can be altered in
409 adulthood in ways that impact the function of the neurons they enmesh, and the variable
410 effect of different CSPGs, hyaluronan and other PNN components to influence plasticity
411 is well-documented¹⁷. PNN composition can also change in response to injury,
412 inflammation, or neurodegeneration in ways that further restrict the plasticity of
413 enmeshed neurons¹⁰. Thus, either a deficiency⁴⁶⁻⁴⁸ or an overabundance¹⁰ of PNNs or
414 individual PNN components can have deleterious effects on circuit behavior and
415 neurological function. As one example, functional recovery after spinal cord injury is

416 limited by “strengthening” of PNNs owing to inflammation and reactive gliosis, such that
417 recovery is improved by PNN disruption¹⁷.

418 In this context, it is notable that diet-induced obesity (DIO) induced by HFD
419 feeding is associated with reactive gliosis involving activation of both microglia and
420 astrocytes in the same ARC area where PNNs are found⁴⁹, and recent work suggests
421 that these glial responses are both necessary and sufficient for obesity in this
422 setting^{50,51}. In this context, our finding of increased tanycyte expression of the
423 hyaluronan receptor CD44 in mice with DIO is of interest because it raises the
424 possibility that environmental exposures in adulthood (*e.g.*, consuming a HFD) can
425 influence signaling between PNN constituents (*e.g.*, hyaluronan) and adjacent cells
426 (*e.g.*, tanycytes) in the ARC-ME. Reports that tanycytes transport circulating leptin into
427 the mediobasal hypothalamus⁵² heighten the potential importance of such interactions.
428 That this obesity-associated increase of tanycyte CD44 content is not observed in *ob/ob*
429 mice despite their severe obesity phenotype is consistent with evidence that
430 hypothalamic gliosis is also not observed in these animals⁵³, presumably reflecting the
431 requirement for an intact leptin signal in this response. These considerations collectively
432 highlight the need for future investigation into the extent to which both PNN composition
433 and ARC neuronal plasticity are altered in models of obesity, diabetes and related
434 metabolic disorders.

435

436 **Methods**

437 *Animals*

438 GAD67-GFP knock-in¹, LepRb-Cre;Ai14 reporter^{2,3}, Npy-GFP⁴, POMC-GFP⁵, and wild-
439 type C57B/6 mice (Jackson Labs), age P60 to P120, were used to characterize
440 neuronal and glial subtypes associated with ARC PNNs. Wild-type C57B/6 mice, age
441 P0 to P90 were used for developmental time-series studies to characterize PNN
442 formation and *Agrp* neuron maturation. To study the effects of leptin deficiency on PNN
443 formation, we used *ob/ob* mice (Jackson Labs). To characterize PNNs in rats, we used
444 the Wistar strain (Harlan). Both sexes were used for all studies. Mice were on 12h:12h
445 light-dark cycle in 5/cage group housing. Animals were perfusion-fixed with saline and
446 4% paraformaldehyde (PFA), the brains were extracted, post-fixed overnight at 4°C,
447 then sectioned using a vibratome (50 μm) or cryostat (12 μm). The Institutional Animal
448 Care and Use Committees at St. Joseph's Hospital and Medical Center and the
449 University of Washington approved all animal procedures.

450

451 *Human Specimens*

452 Three brains (ages 23, 64, and 71 years with postmortem intervals 8, 9, and 12 hours,
453 respectively) were collected at autopsy. Multiple wholemount blocks were dissected
454 from the hypothalamus along the 3rd ventricle from each brain, their positions along the
455 3rd ventricle wall were documented, and the tissue was immersion-fixed in 4% PFA at
456 4°C for 24 hours. All specimens were collected with informed consent and in
457 accordance with the St. Joseph's Hospital and Medical Center Committee on Human
458 Research (IRB no. 10BN159).

459

460 *Stereotactic Intracranial Injections*

461 Animals were head-fixed with ear bars in a custom digital stereotactic rig used to
462 perform unilateral intra-ARC injections of Chondroitinase ABC (10 milliunits in 100
463 nanoliters sterile PBS) at the coordinates (0.3 mm lat, 1.1 mm posterior, 5.6 mm depth)
464 relative to bregma, and sacrificed 48h later. For ICV colchicine administration, 1 ul of
465 colchicine (10 ug/ul in sterile PBS) was injected at (1.3, 0, 1.5) relative to bregma and
466 animals were sacrificed 24h later.

467

468 *Postnatal leptin administration*

469 We crossed ob/+ mice to generate litters containing ob/ob pups. Litters were genotyped
470 at P1-2 and litter sizes were adjusted to 6-8 pups to standardize nutrition during
471 lactation period. Leptin (10 mg/kg i.p.; made available via Dr. A.F. Parlow; National
472 Hormone & Peptide Program, CA) or vehicle was administered on a daily basis at noon
473 from P10-P30 and the animals were euthanized 24 hours after the last injection.

474

475 *Wholemout Dissection*

476 After cervical dislocation, the mouse brain was removed from the skull and 3V
477 wholemouts were freshly dissected using principles similar to those described for LV
478 wholemouts⁵⁴. Briefly, 3V wholemouts were dissected by performing a
479 ventriculotomy of the 3V from ventral to dorsal and rostral to caudal. The exposed
480 ventricle walls were immersion-fixed in 4% PFA at 4°C overnight prior to
481 immunostaining.

482

483 *Immunohistochemistry and Microscopy*

484 For *Wisteria Floribunda* agglutinin (1:500, Sigma L1516) or HA-binding protein (1:50,
485 AMSbio AMS.HKD-BC41) staining, sections were incubated in WFA or HABP in PBS
486 with 0.5% TX followed by streptavidin-Alexa 488 or 561 (1:1000, Invitrogen Molecular
487 Probes) in PBS/0.5% TX, each for 24h at 4°C. For immunostaining, sections were
488 incubated in primary and secondary antibodies in PBS/0.5% TX and 5% normal goat
489 serum for 24-48h at 4°C. Primary antibodies: chicken anti-GFP (1:500, Aves Labs GFP-
490 1020), rabbit anti-dsRed (1:1000, Clontech 632496), rabbit anti-Agrp (1:200, Phoenix
491 Pharmaceuticals H-003-57), rabbit anti-Npy (1:1000, Abcam ab30914), rat anti-
492 somatostatin (1:500, EMD Millipore MAB354), chicken anti-vimentin (1:500, EMD
493 Millipore AB5733), rabbit anti-CD44 (1:1000, Abcam ab157107), and rat anti-
494 phosphacan DSD-1 (1:500, EMD Millipore MAB5790-I). Secondary antibodies:
495 conjugated to Alexa Fluor dyes (goat or donkey polyclonal, 1:500, Invitrogen). Confocal
496 images were taken on a Leica SPE.

497

498 *Electron Microscopy*

499 Adult C57B/6 mice (Jackson Labs) were transcardially perfused with 4% PFA and 0.5%
500 glutaraldehyde (EMS) in 100 mM phosphate buffer (PB). Brains were post-fixed at 4°C
501 overnight, and 50 µm coronal sections were cut on a Leica VT1000 S vibratome. Pre-
502 embedding IHC was performed using WFA (Sigma L1516), amplified with Vectastain
503 Elite ABC kit (Vector Laboratories), and developed with DAB as described previously²⁸.
504 Sections were postfixed in 1% osmium tetroxide for 30 min and then embedded in
505 Durcupan ACM epoxy resin (Fluka, Sigma-Aldrich)⁵⁵. For reconstruction of WFA-
506 labeled neurons, we cut ~200 serial semithin (1.5 µm) sections on an Ultracut UC-6

507 ultramicrotome. Selected semithin sections were glued to resin blocks and detached
508 from glass slides by repeated freeze-thaw. Ultrathin sections (60-80 nm) were then cut
509 and placed on Formvar-coated single-slot grids, stained with lead citrate, and examined
510 at 80 kV on a FEI Tecnai G2 Spirit transmission electron microscope equipped with a
511 Morada CCD digital camera (Olympus).

512

513 *Image Analysis and Quantification*

514 To quantify the proportion of various ARC neuronal subtypes enmeshed by PNNs, we
515 used high resolution confocal z-stacks to reconstruct the ventromedial arcuate region
516 containing PNN structures in two coronal sections containing the median eminence
517 (Bregma -1.7 and -2.0). Only reporter-labelled cells that were completely enmeshed
518 (360°) by WFA-labelled PNN matrix were counted as positive. To analyze the intensity
519 of WFA or CD44 labeling, high resolution confocal z-stacks were volumetrically
520 analyzed in Imaris image analysis software (Bitplane) and voxel intensities throughout
521 the region of interest (e.g. Arc) were determined (intensity unit range, 0-255) and
522 compared across study groups. Raw images were then rendered as 3-dimensional
523 spectral images corresponding to individual voxel intensities. For Agrp fiber density
524 measurements, we used Imaris software to determine the volume of Agrp-labeled
525 positive voxels, above a set intensity threshold, as a fraction of the total volume in the
526 measured region of interest.

527

528 *Statistical Analysis*

529 Descriptive statistics and two-tailed t-tests were computed in GraphPad Prism 7. P-
530 value less than 0.05 was considered statistically significant. Unless otherwise stated,
531 dot plots show dots representing data from individual animals with mean and standard
532 error of the mean shown as bars.

533

534 *Data Availability*

535 All raw images and data analysis presented here are available upon request.

536

537 **Figure Legends**

538

539 **Figure 1.** *Wisteria Floribunda* agglutinin (WFA)-labeling in the ventromedial ARC forms
540 a “collar” around the ME. Diagrams at top show mid-sagittal view (left) and ventral view
541 (right) of the mouse brain with insets showing the location and orientation of panel
542 images.

543 (a-d) WFA-labeled (red) coronal sections through the Arc, starting just rostral to and
544 progressing through the ME, show a concentration of WFA-labeled cells located in the
545 ARC at its junction with the ME. Note that the very intense staining below the ME does
546 not correspond to labeling around neurons, but to the pia around the ME.

547 (e) Higher magnification image of the boxed region in (c) showing the dense cluster of
548 WFA-labeled ARC cells.

549 (f) High magnification Imaris 3-dimensional rendering of an isolated WFA-labeled cell at
550 the periphery of the dense cluster (arrow in c) reveals that WFA labels the soma and
551 proximal processes of ARC cells. Inset shows the raw image.

552 (g-h) Low (g) and high (h) magnification images of PNNs labeled by WFA in the visual
553 cortex, where they have been extensively studied, for comparison. Note similar PNN
554 pattern between (h) and (f) wrapping the soma and proximal process.

555 (i-j) WFA-labeled wholemounts of the ARC viewed from the 3rd ventricle wall en-face (i)
556 or the ventral brain surface (j) reveal the distribution of labeled ARC cells forming a
557 “collar” around the ME, which does not contain labeling. From the ventricular surface
558 view (i), the WFA-labeled ARC cells appear as a continuous band along the ventral
559 margin of the ARC.

560 (k) WFA-labeled coronal section from a wild-type mouse sacrificed 2 days after
561 stereotactic unilateral intra-Arc injection of Chondroitinase ABC, an enzyme that digests
562 chondroitin sulfate carbohydrates.

563 Scale bars: 100 um (a-d, g, i-k), 20 um (e), 10 um (f, h). Images are representative of
564 data from at least 5 animals.

565

566 **Figure 2.** WFA-labelling in the ARC is observed around neuronal soma and neurites by
567 electron microscopy and colocalizes with other major PNN components.

568 (a) Low-power electron micrograph of an ARC section labeled with WFA-DAB shows
569 electron dense DAB deposits surrounding a single ARC neuron (white arrowheads).

570 (b) High-power electron micrograph corresponding to the boxed region in (a) shows
571 WFA-labeling localized to the membrane around the cell soma (white arrowheads) and
572 neurites (white arrows). Note labeling adjacent to an apparent terminal filled with
573 synaptic vesicles (s.v.), as well as the appearance of non-labeled membranes (black
574 arrowheads).

575 (c-e) Confocal images of coronal sections through the ARC stained for other PNN
576 components, including hyaluronic acid using HABP (c, green), the cell surface receptor
577 for hyaluronic acid, CD44 (d, green), and the chondroitin sulfate proteoglycan
578 phosphacan (e, green), show colocalization with WFA (red) in the ARC, providing
579 evidence that ARC WFA-labeling corresponds to PNNs.
580 Scale bars: 2 um (a), 500 nm (b), 100 um (c-e). Images are representative of data from
581 at least 3 animals.

582

583 **Figure 3.** PNNs enmesh GABAergic, LepRb-positive, Agrp/NPY neurons in the Arc.

584 Diagram at top shows mid-sagittal view of mouse brain with location and orientation of
585 panel images.

586 (a) Dot plots show the proportion of individual neuronal subtypes enmeshed by PNNs.

587 Dots in this and all subsequent dot plots represent data from independent animals. The
588 left plot shows the percentage of all PNN-enmeshed ARC cells that belong to a
589 particular neuronal subtype. The right plot shows the percentage of all ARC Npy-GFP
590 or POMC-GFP cells that are enmeshed by PNNs.

591 Low (b, e, h, k, n) and high (c, f, i, l, o) magnification images of coronal sections stained
592 with WFA (red) and antibodies to GFP (green) (b, h, k), dsRed (green) (e), or SST
593 (green) and Agrp (white) (n) show that most PNN-enmeshed cells are GAD67-GFP-
594 positive (GABAergic), LepRb-positive, and NPY-positive, while few enmeshed cells
595 express POMC or SST.

596 (d, g, j, m) High magnification Imaris 3-dimensional surface rendering of isolated ARC
597 PNN-enmeshed cells belonging to the various neuronal subtypes (corresponding to b,

598 e, h, k, respectively) show PNNs wrapping the soma and proximal processes. Insets
599 show raw images. See corresponding supplementary movies 1 and 3 for (d) and (j),
600 respectively.

601 Scale bars: 50 μm (b, e, h, k, n), 20 μm (c, f, i, l, o), 10 μm (d, g, j, m). Images are
602 representative of data from at least 3 animals.

603

604 **Figure 4.** PNN formation in the ARC occurs during the lactation and periweaning
605 period, corresponding with the maturation of *Agrp* neurons.

606 (a-c) Confocal images of coronal sections stained with WFA (red), *Agrp* (green), and
607 dapi (blue) from postnatal wild-type mice at age P10 (a), P21 (b), and P30 (c). PNN
608 staining intensity and ARC *Agrp* fiber density increase in parallel over this time period.

609 (d) Dot plot shows correlated increase in WFA intensity and *Agrp* fiber density in the
610 ARC from P10 to P30, as well at P90. Dots (WFA intensity in red, *Agrp* density in black)
611 represent values from individual animals and horizontal bars represent the mean. WFA
612 intensity is represented by the average over all voxels in the ARC region of interest, with
613 range 0-255. *Agrp* fiber density is measured as the volume of *Agrp*+ voxels divided by
614 the total volume of the ARC region of interest.

615 (e, f) High magnification confocal images of coronal sections stained with WFA (red)
616 and CD44 (green) show that CD44 expression in tanycyte processes and endfeet
617 extends from (e) more medial ME β -tanycytes at P21 (yellow arrowhead indicates cell
618 bodies and yellow arrow indicates endfeet) to (f) more laterally located β -tanycytes with
619 processes penetrating the ARC at P30 (white arrowhead and arrow), concomitant with
620 the increase in PNN intensity over the same period.

621 Scale bars: 100 um (a-c), 50 um (e, f). Images are representative of data from at least 3
622 animals.

623

624 **Figure 5.** Leptin-deficient *ob/ob* mice have impaired PNN formation during postnatal
625 development that can be rescued by leptin administration during the critical period.

626 (a-d) Confocal images of ARC sections from *ob/ob* (b,d) and *ob/+* (a,c) control
627 littermates at P15 (a,b) and P30 (c,d), stained with WFA (red) and Agrp (green), show
628 reduced WFA labeling and apparent disruption of PNN architecture in the ARC.

629 (e-f) Confocal images of ARC sections from *ob/ob* pups that received daily i.p. injections
630 of leptin (f) or vehicle (e) from P10 to P30 before being euthanized for analysis with
631 WFA (red) and Agrp (green). Leptin administration during this critical period appeared
632 to restore WFA labeling intensity and PNN architecture. Insets in (c-f) show higher
633 magnification of the ventromedial ARC region indicated by the arrowhead, revealing an
634 increase in Agrp expression within neuronal soma in leptin deficiency.

635 (g-h) Dot plots show normalized intensity values for WFA in the ARC of P15, P21, and
636 P30 *ob/+* (filled circles) and *ob/ob* (open circles) mice (g), or P30 *ob/ob* mice treated
637 from P10 onward with daily i.p. leptin (red open circle) or vehicle (black open circle)
638 injection (h). Values were normalized to the mean WFA intensity of the control groups
639 (*ob/+* or *ob/ob-veh*). Dots represent values from individual animals. Horizontal bars
640 represent the mean with error bars showing SEM. *two-tailed t-test $p=0.002$, P15;
641 $p=0.0005$, P21; $p<0.0001$, P30; $p=0.02$, P30 rescue.

642 Scale bars: 100 um (a-f), 20 um (insets in c-f). Images are representative of data from
643 each group.

644

645

646 **Figure 6.** Leptin-deficient *ob/ob* mice and DIO mice fed a high fat diet, two rodent
647 models of obesity and glucose intolerance, exhibit altered ARC PNNs or PNN
648 constituents.

649 (a, b) High magnification confocal images (a) of coronal sections stained with WFA and
650 corresponding Imaris spectral images (b) showing voxel intensity from C57B/6 wt, *obob*,
651 chow-fed, or high-fat diet (HFD) -fed mice. Adult *obob* mice exhibited increased ARC
652 PNN intensity compared to wt, but there was no difference between mice fed chow and
653 HFD.

654 (c, d) High magnification confocal images (c) of coronal sections stained with CD44 and
655 corresponding Imaris spectral images (d) showing voxel intensity from C57B/6 wt, *obob*,
656 chow fed, or HFD fed mice. DIO mice fed HFD exhibited increased tanycyte CD44
657 expression compared with chow fed mice, with no difference observed between wt and
658 *obob* mice. Note that wt and *obob* mice are age-matched 3 mo old mice fed standard
659 chow diet. Chow and HFD mice were C57B/6 wt mice that were fed either chow or hfd
660 for 12 weeks (beginning at age 3 mo. and sacrificed at age 6 mo.). Spectral reference
661 line shown in (b) with intensity range 0 to 150 and (d) with range 30 to 150.

662 (e) Dot plots show normalized intensity values for CD44 and WFA in the ARC of wt and
663 *obob* mice (left) and chow and HFD mice (right). Values were normalized to the mean
664 WFA or CD44 intensity of the control groups (wt or chow). Dots represent values from
665 individual animals. Horizontal bars represent the mean with error bars showing SEM.

666 *two-tailed t-test $p=0.004$ for WFA *obob* v. wt, $p=0.007$ for CD44 HFD v. chow.

667 Scale bars: 50 um (a), 100 um (c). Images are representative of data from each group.

668

669 **Figure 7.** PNNs enmesh NPY+ neurons in the human Arc.

670 (a) Multi-tile confocal image of a coronal section through the human mediobasal

671 hypothalamus stained with WFA (red), NPY (green), and dapi (blue). Boxed region

672 shows location of image in (b).

673 (b) High magnification image shows many PNN-enmeshed NPY+ cells in the human

674 Arc. Arrow indicates cell shown in (c).

675 (c) High magnification Imaris 3-dimensional surface rendering of human ARC PNN-

676 enmeshed NPY+ cell shows PNNs wrapping the soma and proximal processes, as in

677 the mouse ARC and PNN-enmeshed cells in other brain areas. Inset shows raw image

678 with WFA (red) and NPY (green). See corresponding supplementary movie 4.

679 Scale bars: 2 mm (a), 100 um (b), 10 um (c). Images of representative of data from 2

680 human specimens.

681

682 **Supplementary Figure 1.** Tiled panoramic confocal image of a coronal section at the

683 level of the ARC stained with WFA (top), and corresponding serial coronal sections

684 through the hypothalamus from the optic chiasm (oc) to the infundibular recess (bottom

685 row), reveal a specific concentration of PNN enmeshed cells in the ventromedial ARC at

686 its junction with the ME. Scale bar: 500 um. Images are representative of data from at

687 least 5 animals.

688

689 **Supplementary Figure 2.** Low- (a,c,e) and high-power (b,d,f correspond to boxed
690 regions in low-power images) electron micrographs showing comparative ultrastructural
691 distribution of WFA-DAB deposits around neurons in the cortex (a,b), hippocampus
692 (c,d), and ARC (e,f) reveal very similar patterns of labeling localized to the soma and
693 adjacent neurites in all 3 regions. Scale bars: 2 μ m (a,c,e), 500 nm (b,d,f). Images are
694 representative of data from at least 3 animals.

695

696 **Supplementary Figure 3.** Serial coronal sections (a) through the hypothalamus from
697 the optic chiasm (oc) to the infundibular recess stained with WFA (red) and CD44
698 (green) reveal regional colocalization of the PNN constituent hyaluronan receptor CD44
699 and PNNs in the ventromedial Arc-ME. Low- (b) and high-magnification (c) images of a
700 coronal section stained with WFA (red), CD44 (green), and vimentin (magenta) reveal
701 that CD44 is expressed on β -tanyocyte processes and their endfeet (arrow), but not on α -
702 tanyocyte processes or endfeet (arrowhead).

703 Scale bar: 500 μ m (a), 100 μ m (b), 50 μ m (c). Images are representative of data from at
704 least 3 animals.

705

706 **Supplementary Figure 4.** PNNs enmesh GABAergic interneurons in the visual cortex.
707 (a) Confocal image of a coronal section through the primary visual cortex of a GAD67-
708 GFP mouse stained with WFA (red) and GFP antibody (green) shows many PNN
709 enmeshed GABAergic interneurons in layer II-III. Arrow indicates cell shown in (b).
710 (b) High magnification confocal image (left) and Imaris 3-dimensional surface rendering
711 (right) of an isolated PNN-enmeshed GABAergic interneuron shows PNNs wrapping the

712 soma and proximal processes. Scale bars: 100 um (a), 20 um (b). Images are
713 representative of data from at least 5 animals.

714

715 **Supplementary Figure 5.** Dot plot shows normalized intensity values for WFA in the
716 ARC and V1 of wt and *obob* mice. Increased WFA intensity in *obob* mice was seen in
717 the Arc, but not in V1. Values were normalized to the mean WFA intensity of wt ARC or
718 V1. Dots represent values from individual animals. Horizontal bars represent the mean
719 with error bars showing SEM.

720

721 **Supplementary Figure 6.** PNNs are conserved across the mouse, rat, and human Arc.
722 (a, d, g) Low magnification confocal images of coronal sections from mouse (a), rat (d),
723 and human (g), stained with WFA and GFP (Npy-GFP mice in (a)) or NPY (d, g).
724 Across species, the ARC displays more intense WFA-labeling than the nearby VMN,
725 where WFA labeling is diffuse. This is confirmed in higher magnification confocal
726 images of the ARC (b, e, h) and VMN (c, f, i). Scale bars: 500 um (a, d), 20 um (b, c, e,
727 f, h, i), 4 mm (g).

728

729 **Supplementary Movie 1.** Imaris 3-dimensional surface rendering of an isolated PNN-
730 enmeshed (red) GAD67-GFP+ ARC neuron (green).

731 **Supplementary Movie 2.** Imaris 3-dimensional surface rendering of an isolated PNN-
732 enmeshed (red) GAD67-GFP+ V1 interneuron (green).

733 **Supplementary Movie 3.** Imaris 3-dimensional surface rendering of an isolated PNN-
734 enmeshed (red) Npy-GFP+ ARC neuron (green).

735 **Supplementary Movie 4.** Imaris 3-dimensional surface rendering of an isolated PNN-
736 enmeshed (red) NPY+ human ARC neuron (green).

737

738 **References**

739

- 740 1 Tamamaki, N. *et al.* Green fluorescent protein expression and colocalization with
741 calretinin, parvalbumin, and somatostatin in the GAD67-GFP knock-in mouse. *J Comp*
742 *Neurol* **467**, 60-79 (2003).
- 743 2 Leshan, R. L., Bjornholm, M., Munzberg, H. & Myers, M. G., Jr. Leptin receptor signaling
744 and action in the central nervous system. *Obesity* **14 Suppl 5**, 208S-212S,
745 doi:10.1038/oby.2006.310 (2006).
- 746 3 Madisen, L. *et al.* A robust and high-throughput Cre reporting and characterization
747 system for the whole mouse brain. *Nat Neurosci* **13**, 133-140, doi:10.1038/nn.2467
748 (2010).
- 749 4 van den Pol, A. N. *et al.* Neuromedin B and gastrin-releasing peptide excite arcuate
750 nucleus neuropeptide Y neurons in a novel transgenic mouse expressing strong Renilla
751 green fluorescent protein in NPY neurons. *J Neurosci* **29**, 4622-4639,
752 doi:10.1523/JNEUROSCI.3249-08.2009 (2009).
- 753 5 Cowley, M. A. *et al.* Leptin activates anorexigenic POMC neurons through a neural
754 network in the arcuate nucleus. *Nature* **411**, 480-484, doi:10.1038/35078085 (2001).
- 755 6 Hensch, T. K. Critical period plasticity in local cortical circuits. *Nat Rev Neurosci* **6**, 877-
756 888 (2005).
- 757 7 Wiesel, T. N. & Hubel, D. H. Single-Cell Responses in Striate Cortex of Kittens Deprived of
758 Vision in One Eye. *J. Neurophysiol.* **26**, 1003-1017 (1963).
- 759 8 Pizzorusso, T. *et al.* Reactivation of ocular dominance plasticity in the adult visual cortex.
760 *Science* **298**, 1248-1251, doi:10.1126/science.1072699 (2002).
- 761 9 Carulli, D. *et al.* Animals lacking link protein have attenuated perineuronal nets and
762 persistent plasticity. *Brain* **133**, 2331-2347, doi:10.1093/brain/awq145 (2010).
- 763 10 Kwok, J. C., Dick, G., Wang, D. & Fawcett, J. W. Extracellular matrix and perineuronal
764 nets in CNS repair. *Dev Neurobiol* **71**, 1073-1089, doi:10.1002/dneu.20974 (2011).
- 765 11 Balmer, T. S., Carels, V. M., Frisch, J. L. & Nick, T. A. Modulation of perineuronal nets and
766 parvalbumin with developmental song learning. *J Neurosci* **29**, 12878-12885,
767 doi:10.1523/JNEUROSCI.2974-09.2009 (2009).
- 768 12 Gogolla, N., Caroni, P., Luthi, A. & Herry, C. Perineuronal nets protect fear memories
769 from erasure. *Science* **325**, 1258-1261, doi:10.1126/science.1174146 (2009).
- 770 13 Nowicka, D., Soulsby, S., Skangiel-Kramska, J. & Glazewski, S. Parvalbumin-containing
771 neurons, perineuronal nets and experience-dependent plasticity in murine barrel cortex.
772 *The European journal of neuroscience* **30**, 2053-2063, doi:10.1111/j.1460-
773 9568.2009.06996.x (2009).

774 14 Beurdeley, M. *et al.* Otx2 binding to perineuronal nets persistently regulates plasticity in
775 the mature visual cortex. *J Neurosci* **32**, 9429-9437, doi:10.1523/JNEUROSCI.0394-
776 12.2012 (2012).

777 15 Miyata, S., Komatsu, Y., Yoshimura, Y., Taya, C. & Kitagawa, H. Persistent cortical
778 plasticity by upregulation of chondroitin 6-sulfation. *Nat Neurosci* **15**, 414-422, S411-
779 412, doi:10.1038/nn.3023 (2012).

780 16 Maeda, N. Structural variation of chondroitin sulfate and its roles in the central nervous
781 system. *Cent Nerv Syst Agents Med Chem* **10**, 22-31 (2010).

782 17 Miyata, S. & Kitagawa, H. Formation and remodeling of the brain extracellular matrix in
783 neural plasticity: Roles of chondroitin sulfate and hyaluronan. *Biochim Biophys Acta*
784 **1861**, 2420-2434, doi:10.1016/j.bbagen.2017.06.010 (2017).

785 18 Kamitakahara, A., Bouyer, K., Wang, C. H. & Simerly, R. A critical period for the trophic
786 actions of leptin on AgRP neurons in the arcuate nucleus of the hypothalamus. *J Comp*
787 *Neurol* **526**, 133-145, doi:10.1002/cne.24327 (2018).

788 19 Bouret, S. G., Draper, S. J. & Simerly, R. B. Trophic action of leptin on hypothalamic
789 neurons that regulate feeding. *Science* **304**, 108-110, doi:10.1126/science.1095004
790 (2004).

791 20 Ahima, R. S., Prabakaran, D. & Flier, J. S. Postnatal leptin surge and regulation of
792 circadian rhythm of leptin by feeding. Implications for energy homeostasis and
793 neuroendocrine function. *The Journal of clinical investigation* **101**, 1020-1027,
794 doi:10.1172/JCI1176 (1998).

795 21 Bouyer, K. & Simerly, R. B. Neonatal leptin exposure specifies innervation of
796 presympathetic hypothalamic neurons and improves the metabolic status of leptin-
797 deficient mice. *J Neurosci* **33**, 840-851, doi:10.1523/JNEUROSCI.3215-12.2013 (2013).

798 22 Baquero, A. F. *et al.* Developmental switch of leptin signaling in arcuate nucleus
799 neurons. *J Neurosci* **34**, 9982-9994, doi:10.1523/JNEUROSCI.0933-14.2014 (2014).

800 23 Bouret, S. G. *et al.* Hypothalamic neural projections are permanently disrupted in diet-
801 induced obese rats. *Cell metabolism* **7**, 179-185, doi:10.1016/j.cmet.2007.12.001 (2008).

802 24 Glavas, M. M. *et al.* Early overnutrition results in early-onset arcuate leptin resistance
803 and increased sensitivity to high-fat diet. *Endocrinology* **151**, 1598-1610,
804 doi:10.1210/en.2009-1295 (2010).

805 25 Vogt, M. C. *et al.* Neonatal insulin action impairs hypothalamic neurocircuit formation in
806 response to maternal high-fat feeding. *Cell* **156**, 495-509, doi:10.1016/j.cell.2014.01.008
807 (2014).

808 26 Bayol, S. A., Simbi, B. H. & Stickland, N. C. A maternal cafeteria diet during gestation and
809 lactation promotes adiposity and impairs skeletal muscle development and metabolism
810 in rat offspring at weaning. *J Physiol* **567**, 951-961, doi:10.1113/jphysiol.2005.088989
811 (2005).

812 27 Gorski, J. N., Dunn-Meynell, A. A., Hartman, T. G. & Levin, B. E. Postnatal environment
813 overrides genetic and prenatal factors influencing offspring obesity and insulin
814 resistance. *Am J Physiol Regul Integr Comp Physiol* **291**, R768-778,
815 doi:10.1152/ajpregu.00138.2006 (2006).

816 28 Carstens, K. E., Phillips, M. L., Pozzo-Miller, L., Weinberg, R. J. & Dudek, S. M.
817 Perineuronal Nets Suppress Plasticity of Excitatory Synapses on CA2 Pyramidal Neurons.
818 *J Neurosci* **36**, 6312-6320, doi:10.1523/JNEUROSCI.0245-16.2016 (2016).

819 29 Koppe, G., Bruckner, G., Hartig, W., Delpech, B. & Bigl, V. Characterization of
820 proteoglycan-containing perineuronal nets by enzymatic treatments of rat brain
821 sections. *Histochem J* **29**, 11-20 (1997).

822 30 Schwartz, M. W. *et al.* Obesity Pathogenesis: An Endocrine Society Scientific Statement.
823 *Endocr Rev* **38**, 267-296, doi:10.1210/er.2017-00111 (2017).

824 31 Backberg, M., Collin, M., Ovesjo, M. L. & Meister, B. Chemical coding of GABA(B)
825 receptor-immunoreactive neurones in hypothalamic regions regulating body weight. *J*
826 *Neuroendocrinol* **15**, 1-14 (2003).

827 32 Morrison, C. D., Morton, G. J., Niswender, K. D., Gelling, R. W. & Schwartz, M. W. Leptin
828 inhibits hypothalamic Npy and Agrp gene expression via a mechanism that requires
829 phosphatidylinositol 3-OH-kinase signaling. *Am J Physiol Endocrinol Metab* **289**, E1051-
830 1057, doi:10.1152/ajpendo.00094.2005 (2005).

831 33 McRae, P. A., Rocco, M. M., Kelly, G., Brumberg, J. C. & Matthews, R. T. Sensory
832 deprivation alters aggrecan and perineuronal net expression in the mouse barrel cortex.
833 *J Neurosci* **27**, 5405-5413, doi:10.1523/JNEUROSCI.5425-06.2007 (2007).

834 34 Nakamura, M. *et al.* Expression of chondroitin sulfate proteoglycans in barrel field of
835 mouse and rat somatosensory cortex. *Brain Res* **1252**, 117-129,
836 doi:10.1016/j.brainres.2008.11.022 (2009).

837 35 Dityatev, A. *et al.* Activity-dependent formation and functions of chondroitin sulfate-rich
838 extracellular matrix of perineuronal nets. *Dev Neurobiol* **67**, 570-588,
839 doi:10.1002/dneu.20361 (2007).

840 36 Luquet, S., Perez, F. A., Hnasko, T. S. & Palmiter, R. D. NPY/AgRP neurons are essential
841 for feeding in adult mice but can be ablated in neonates. *Science* **310**, 683-685,
842 doi:10.1126/science.1115524 (2005).

843 37 Xu, J. *et al.* Genetic identification of leptin neural circuits in energy and glucose
844 homeostases. *Nature* **556**, 505-509, doi:10.1038/s41586-018-0049-7 (2018).

845 38 de Winter, F. *et al.* The Chemorepulsive Protein Semaphorin 3A and Perineuronal Net-
846 Mediated Plasticity. *Neural Plast* **2016**, 3679545, doi:10.1155/2016/3679545 (2016).

847 39 Catalano, P. M. *et al.* Perinatal risk factors for childhood obesity and metabolic
848 dysregulation. *Am J Clin Nutr* **90**, 1303-1313, doi:10.3945/ajcn.2008.27416 (2009).

849 40 Lumey, L. H., Stein, A. D. & Susser, E. Prenatal famine and adult health. *Annu Rev Public*
850 *Health* **32**, 237-262, doi:10.1146/annurev-publhealth-031210-101230 (2011).

851 41 Barker, D. J. P. *Fetal and Infant Origins of Adult Disease*. (British Medical Journal, 1992).

852 42 Ravelli, G. P., Stein, Z. A. & Susser, M. W. Obesity in young men after famine exposure in
853 utero and early infancy. *N Engl J Med* **295**, 349-353,
854 doi:10.1056/NEJM197608122950701 (1976).

855 43 Ravelli, A. C. *et al.* Glucose tolerance in adults after prenatal exposure to famine. *Lancet*
856 **351**, 173-177 (1998).

857 44 Painter, R. C., Roseboom, T. J. & Bleker, O. P. Prenatal exposure to the Dutch famine and
858 disease in later life: an overview. *Reprod Toxicol* **20**, 345-352,
859 doi:10.1016/j.reprotox.2005.04.005 (2005).

860 45 Vickers, M. H. *et al.* Neonatal leptin treatment reverses developmental programming.
861 *Endocrinology* **146**, 4211-4216, doi:10.1210/en.2005-0581 (2005).

862 46 Saghatelyan, A. K. *et al.* Reduced perisomatic inhibition, increased excitatory
863 transmission, and impaired long-term potentiation in mice deficient for the extracellular
864 matrix glycoprotein tenascin-R. *Mol Cell Neurosci* **17**, 226-240,
865 doi:10.1006/mcne.2000.0922 (2001).

866 47 Bukalo, O., Schachner, M. & Dityatev, A. Modification of extracellular matrix by
867 enzymatic removal of chondroitin sulfate and by lack of tenascin-R differentially affects
868 several forms of synaptic plasticity in the hippocampus. *Neuroscience* **104**, 359-369
869 (2001).

870 48 Hylin, M. J., Orsi, S. A., Moore, A. N. & Dash, P. K. Disruption of the perineuronal net in
871 the hippocampus or medial prefrontal cortex impairs fear conditioning. *Learn Mem* **20**,
872 267-273, doi:10.1101/lm.030197.112 (2013).

873 49 Thaler, J. P. *et al.* Obesity is associated with hypothalamic injury in rodents and humans.
874 *The Journal of clinical investigation* **122**, 153-162, doi:10.1172/JCI59660 (2012).

875 50 Douglass, J. D., Dorfman, M. D., Fasnacht, R., Shaffer, L. D. & Thaler, J. P. Astrocyte
876 IKKbeta/NF-kappaB signaling is required for diet-induced obesity and hypothalamic
877 inflammation. *Molecular metabolism* **6**, 366-373, doi:10.1016/j.molmet.2017.01.010
878 (2017).

879 51 Valdearcos, M. *et al.* Microglial Inflammatory Signaling Orchestrates the Hypothalamic
880 Immune Response to Dietary Excess and Mediates Obesity Susceptibility. *Cell*
881 *metabolism* **26**, 185-197 e183, doi:10.1016/j.cmet.2017.05.015 (2017).

882 52 Balland, E. *et al.* Hypothalamic tanycytes are an ERK-gated conduit for leptin into the
883 brain. *Cell metabolism* **19**, 293-301, doi:10.1016/j.cmet.2013.12.015 (2014).

884 53 Gao, Y. *et al.* Hormones and diet, but not body weight, control hypothalamic microglial
885 activity. *Glia* **62**, 17-25, doi:10.1002/glia.22580 (2014).

886 54 Mirzadeh, Z., Doetsch, F., Sawamoto, K., Wichterle, H. & Alvarez-Buylla, A. The
887 subventricular zone en-face: wholemount staining and ependymal flow. *J Vis Exp*,
888 doi:1938 [pii]
889 10.3791/1938 (2010).

890 55 Doetsch, F., Garcia-Verdugo, J. M. & Alvarez-Buylla, A. Cellular composition and three-
891 dimensional organization of the subventricular germinal zone in the adult mammalian
892 brain. *J. Neurosci.* **17**, 5046-5061 (1997).

893